Materials Today Energy 9 (2018) 345–358

Contents lists available at ScienceDirect

Materials Today Energy

journal homepage: www.journals.elsevier.com/materials-today-energy/

Structure and photoactivity for hydrogen production of CdS nanorods modified with In, Ga, Ag-In and Ag-Ga and prepared by solvothermal method

E. Soto [a], F. Vaquero [a], N. Mota [a], S. Fateixa [b], T. Trindade [b], R.M. Navarro [a, *], J.L.G. Fierro [a]

[a] Instituto de Catálisis y Petroleoquímica (CSIC), C/Marie Curie 2, 28049, Madrid, Spain
[b] Department of Chemistry-CICECO University of Aveiro, 3810-193 Aveiro, Portugal

ARTICLE INFO

Article history:
Received 6 March 2018
Received in revised form
18 May 2018
Accepted 16 June 2018

Keywords:
CdS
Ag
In
Ga
Water splitting
Hydrogen
Photocatalysis
Solvothermal

ABSTRACT

This work studies the variation in the photocatalytic properties of CdS derived from the insertion of In, Ga, Ag-In and Ag-Ga in the CdS lattice through solvothermal methodology. Solvothermal synthesis of CdS-M photocatalysts has been succesful for the insertion of Ga^{3+}, In^{3+}, Ga^{3+}/Ag^{+} and In^{3+}/Ag^{+} into the hexagonal crystal lattice of one-dimensional CdS. The insertion of In, Ga, Ag-In and Ag-Ga modifies the band gap and the relative position of $E_{VB.}$ CdS modified with In^{3+} or Ga^{3+} shows an increase in the band gap and upshift in the relative position of the valence band energy which leads to a low efficiency hydrogen production. The co-addition of Ag^{+}-In^{3+} or Ag^{+}-Ga^{3+} favours the insertion of Ag^{+} ions into the CdS lattice with narrower band gap. Of all the co-substituted photocatalysts, the CdS-AgGa was the only one that showed a higher photoactivity with respect to the CdS. The increase in the photoactivity of the CdS-AgGa photocatalyst is related to the band gap narrowing and downshift in the relative position of the valence band energy which enhance their visible light absorption and potential for oxidation. The CdS-AgGa photocatalyst shows small segregation of metallic Ag nanoparticles at the surface which also assist in the photoactivity of the sample.

1. Introduction

The photocatalytic water splitting process using visible light is an interesting way to produce renewable hydrogen [1]. Different types of photocatalysts e.g. oxides, sulfides, oxynitrides and oxysulfides, have been developed over the past 40 years for this process [2–4]. However their efficiency for hydrogen production under visible light still needs to be improved before it can be applied. Among the photocatalysts developed for hydrogen evolution under visible light, CdS is one of the most studied [5–8] because of the energy position of the conduction and valence bands and its narrow band gap (2.4eV) which enables a good use of the solar spectrum. Several research studies into CdS have been presented in the literature with the aim of improving its photocatalytic efficiency by controlling its electronic, microstructural, morphological and surface properties because these factors define its photoactivity [9e12]. Among the available strategies for the enhancement of hydrogen production are the use of co-catalysts [13,14], the hybridation with highly conductive materials to form heterojunctions [15e17], doping with transition metals [18] or forming solid solutions [19]. Two of the most studied strategies for the improvement of the efficiency of the CdS photocatalysts are related to the tuning of its band-gap energy by means of cation doping, and by the deposition of co-catalysts on its surface to reduce the activation energy for gas evolution [20,21]. These strategies must be combined with the control of the synthesis of CdS to adjust its crystallinity, size and morphology at the nanometric scale because these characteristics havev a strong influence on the photoactivity. Regarding the synthesis of CdS, one dimensional (1D) nanostructures e.g. nanorods, nanowires and nanofibers, have attracted much attention arising from their high activity which comes from the confinement effects associated with their high surface to volume ratio. Several synthesis methods enable 1D nanomorphologies: e.g. electrochemical synthesis, chemical vapor deposition, colloidal micellar methods, vapor-liquid-solid (VLS) assisted-methods, hydrothermal and solvothermal, among others. The solvothermal method uses polyamines as structure directing agents that allows the control of the nanostructure of the CdS

* Corresponding author.
E-mail address: r.navarro@icp.csic.es (R.M. Navarro).

https://doi.org/10.1016/j.mtener.2018.06.009

particles in the form of 1D nanomorphologies [22–24]. Ethylenediamine (EDA) is the most frequently used polyamine solvent because it favours the growth of CdS and has a preferential direction by means of the coordination of EDA with the Cd^{2+} ions. In addition to the solvent, other solvothermal variables such as temperature, precursors and time, are also important factors that control the crystallinity and morphology of the CdS nanostructures.

As indicated above the replacement of Cd^{2+} ions in its crystal lattice with other transition metal ions is a versatile strategy for the modification of its electronic band structure. This modification can create intermediate energy states through the formation of solid solutions or interstitial doping that improves absorption in the visible range and/or the potential for water-oxidation/reduction processes, changes to the electrical properties or improving the chemical stability by injecting the holes into the formed acceptor energy levels thereby reducing photocorrosion. The doping of the CdS by metal cations has been the subject of many studies where the cations are introduced in its crystal lattice by chemical vapor deposition, sol–gel, coprecipitation or plasma implantation. Usually metal doping in CdS is performed by replacement of the Cd^{2+} ions, substitutionally or interstitially, with transition metal cations e.g. Ni^{2+}, Zn^{2+}, Co^{2+}, Mn^{2+}, with charge and ionic radii similar to Cd^{2+} (0.85 Å). Enhanced photoactivity and stability of Mn-, Cu-, Ni- and Zn-doped CdS for visible-light hydrogen production has been extensively documented in the literature showing the effectiveness of this process in improving the efficiency by inter-semiconductor transfer steps in the doped photocatalysts [25–28].

Metal doping of CdS with the aliovalent ions In^{3+} and Ga^{3+} has also been proposed as a doping strategy to improve its photoactivity, taking into account the possibility offered by these cations to tune the band structure of CdS in order to improve the efficiency for the absorption and use of solar light [29–32]. The modification of the photoactivity of CdS with these metal doping agents has been poorly studied, and the effect of doping with In and Ga on the structure and photoactivity of CdS remains unclear [33]. Yang et al. reported the successful preparation of interstitial Ga-doped CdS which showed an enhancement in photoactivity attributed to the band gap narrowing, the widening of the valence band, and an indirect semiconductor nature [42]. Sasikala et al. reported the enhanced activity of the indium doped supported CdS system due to the increased lifetime of the charge carriers and the relatively improved optical absorption of this system [33]. In spite of the improvements associated with the replacement of the Cd^{2+} ions with the M^{3+} aliovalent ions, the replacement can also cause charge imbalance and vacancies that may negatively affect the photoactivity of the substituted CdS. In order to avoid the drawbacks associated with the individual substitution with aliovalent ions in the structure of CdS, the co-substitution of M^{+} and M^{3+} ions was also proposed as a strategy for altering the electronic band structure of CdS because the insertion of both aliovalent cations results in the balancing of charge minimizing vacancies [34,35]. Co-substitution of M^{3+} ions with Ag^{+} could be of special interest taking into account the possible formation of solid solutions between $AgMS_2$ and sulphides with a wurtzite structure that facilitates the insertion of both cations in the CdS lattice [36–38]. In addition, an enhancement in the recombination life-time of carriers could be achieved on Ag-doped CdS associated with the surface plasmon resonance (SPR) which act as photosensitizers to strengthen the absorption of CdS.

In line with the above, this work was undertaken with the aim of modifying the photocatalytic properties of CdS by means of the mono-substitution of CdS with In^{3+} and Ga^{3+} and the co-substitution with Ag^{+}-Ga^{3+} and Ag^{+}-In^{3+}. The possibility offered by these cations to change the band structure of CdS in order to improve the efficiency for the absorption and use of solar light was taken into consideration. The strategy of the modification of the CdS with aliovalent cations was combined with the control of the nanosynthesis of the CdS by solvothermal methodology that enables customizing the crystallinity and morphology at the nanometric scale. Textural, structural and surface properties of the substituted CdS samples have been determined in order to analyse the role of aliovalent ions during the synthesis, and their effect on the final morphological, optical and structural properties of the modified CdS samples.

2. Experimental

2.1. Solvothermal synthesis of CdS-M (M = In, Ga, AgIn, AgGa)

Two CdS-M series corresponding to the mono-substitution of CdS with In^{3+} and Ga^{3+} and the co-substitution with Ag^{+}-Ga^{3+} and Ag^{+}-In^{3+} were prepared according to the stoichiometry $M_{0.05}$-$Cd_{0.95}S$ ($M = In^{3+}$, Ga^{3+}) and $Ag_{0.05}M_{0.05}$-$Cd_{0.9}S$ ($M = In^{3+}$, Ga^{3+}). Cadmium chloride ($CdCl_2$), silver acetate ($Ag(CH_3COO)$), indium acetate ($In(CH_3COO)_3$), gallium chloride ($GaCl_3$) and elemental sulfur (S) were used as precursors in the synthesis of the CdS-M samples. As described in our previous work [7–9] the solvothermal synthesis uses a Teflon-lined stainless steel autoclave filled with ethylenediamine (EDA) to 80% of its capacity with metallic salts in a Cd/M (M = In, Ga) molar ratio 1/0.05. In order to promote the complete precipitation of the metal sulfides, an excess of elemental sulfur was added in a Cd/S molar ratio equal to 1/3. The autoclave was heated at 120 °C for 12 h and then cooled to room temperature. The solids obtained were washed with distilled water and ethanol and collected by centrifugation. Finally the solids were dried under vacuum at 70 °C for 2 h. According to the aliovalent cation used, the samples were labelled: CdS-M (M = In, Ga, AgIn and AgGa). A non-substituted CdS reference sample was also synthesized using this methodology.

2.2. Physicochemical characterization

The chemical composition of the CdS-M photocatalysts was determined by total X-ray fluorescence analysis (TXRF) using a benchtop S2 PicoFox TXRF spectrometer (Bruker Nano GmbH, Berlin, Germany), equipped with a molybdenum X-ray source working at 50 kV and 600 A, a multilayer monochromator with 80% reflectivity at 17.5 keV (Mo K), an XFlash SDD detector with an effective area of 30 mm^2, and an energy resolution better than 150 eV for Mn K. The beam impacts over the sample and is reflected almost entirely, penetrating approximately only 10–15 nm in the sample.

The specific surface area of photocatalyst samples were determined by the BET method to the N_2 adsorption/desorption isotherms measured at liquid nitrogen at −196 °C on a Micromeritics TRISTAR 3000 instrument over samples which had previously been degassed under vaccum at 70 °C for 2 h, to remove the gases and moisture adsorbed on the surface of the samples. The specific surface area of all the samples have been calculated within the relative pressure $0.05 < P/Po < 0.30$.

The crystalline characteristics of CdS-M photocatalysts were evaluated by X-ray Powder Diffraction (XRD) using an X'Pert Pro PANalytical polycrystal diffractometer with a X'Celerator RTMS detector and nickel-filtered Cu Kα radiation ($\lambda = 0.15406$ nm, 45 kV, 40 mA) under constant instrument parameters. The scanning range was established between Bragg angles 20 ° and 90° (2θ) with a step size 0.0335° during a continuous scan. The estimation of the size of the crystalline domains of the CdS-M samples (Dp) was carried out by applying the Scherrer equation from the broadening of the (002) reflections of the hexagonal CdS-M phase. In this study the

Williamson-Hall analysis was carried out for the estimation of the lattice strains of the CdS-M nanostructures which are a consequence of the insertion of aliovalent cations on the CdS lattice. By plotting eq. (1) (below) for the three main reflection planes of the hexagonal CdS-M, it is possible to quantify the microstrain lattice parameter ( ):

$$cos \quad = \frac{K}{D} + 4 \quad \cdot sin \tag{1}$$

where β is the broadening of the diffracted peak, K is a shape factor close to unity, λ is the X-ray wavelength, D is the crystallite size and is the slope of the linear fit of the plot.

Raman spectra of all the samples were obtained using a combined Raman-AFM-SNOM confocal microscope WITec alpha300 RAS+ (WITec, Ulm, Germany). An Nd:YAG laser operated at 532 nm was used as the excitation source with the power set at 1 mW. Raman spectra were collected with a 100 × objective lens with an acquisition time of 2 s and 10 acquisitions. Raman imaging experiments were performed by raster-scanning the laser beam over the samples and accumulating a full Raman spectrum at each pixel. Raman images were constructed by integrating over specific Raman bands using WITec software for data evaluation and processing.

Surface analyses of the CdS-M samples were obtained from X-ray photoelectron spectra (XPS) obtained using a VG Escalab 200R spectrometer equipped with a hemispherical electron analyser and Mg Kα radiation (1253.6 eV). The Cd 3d, Ga 2p, In 3d and Ag 3d core-level spectra in the CdS-M samples were recorded. The spectra for the regions of interest were curve fitted using the *XPS Peak software*. Curve fitting was performed using Gaussian-Lorentzian (90% G-10% L) shapes with a Shirley background. Atomic ratios were computed from the intensity ratios normalized by atomic sensitivity factors [39].

The nanomorphological characteristics of the CdS-M photocatalysts were determined from transmission electron microscopy (TEM) and high-resolution transmission electron microscopy (HRTEM) with a TEM/STEM JEOL 2100F electron microscope operating at a 200 kV accelerating voltage with a Field Emission Gun (FEG), obtaining a point resolution of 0.19 nm.

Diffuse reflectance measurements of the CdS-M photocatalysts were performed in a UV-vis-NIR Varian Cary 5000 spectrometer with the double beam and double shutter synchronized electronically. The sources were deuterium (UV) and halogen quartz. The detectors were a multiplier and PbS detector refrigerated for the NIR area. By plotting the Kubelka-Munk Function F(R) against the photonic energy (hυ) an approximated profile of the absorption properties of the samples was obtained. The band gap size was obtained from Tauc plot tracing a tangent line parallel to the slope of the curve to the x-axis. The wavelength obtained was converted to energy units according to Eph = hc/ λ, where Eph is the photonic energy, h is the Planck constant, c the speed of light, and λ the photon wavelength. Defects can cause a tailing effect on UV–vis spectra, Urbach tails [29,40] due to the presence of localized electronic states near the band gap region in the UV–vis spectra were observed. By applying the Urbach law (eq. (2) below) it is possible to quantify the density of defects near the band gap through the Urbach energy parameter, Eu:

$$\ln(F(R)) = A + \quad \frac{1}{Eu} \quad \cdot h\nu \tag{2}$$

where F(R) is the Kubelka-Munk function, h is the Planck constant, ν the speed of light and Eu is the inverse of the slope of the straight line of the plot in meV.

Ultraviolet photoelectron spectroscopy analyses (UPS) were performed to determine the valence band energy position (VBM) of CdS-M samples. The measurements were acquired using a SPECS GmbH spectrometer with UHV system (ca. 10^{-10} mbar) equipped with an energy analyzer PHOIBOS 150 9MCD. The UPS spectra were obtained by applying a monochromatic radiation He (I) radiation (hυ = 21.2 eV) with a pass energy 2eV and a step energy 0.02 eV. The relative energy position of the valence band maximum (VBM) with respect to the conduction band minimum (CBM) was calculated by applying the eqs. (3)–(5) below) [41]:

$$= h \quad - E_{cutoff} \tag{3}$$

$$VBM = h \quad - \quad E_{cutoff} + E_{VBM} \tag{4}$$

$$CBM = VBM + BG \tag{5}$$

where Φ is the work function, hυ corresponds to the radiation energy of He (I), E_{cutoff} is the secondary edge region and E_{VBM} is the energy level of the valence band obtained from the intersection of the tangent line to the slope with x-axis in the UPS spectra.

The photoluminescence (PL) spectra of CdS-M photocatalysts were recorded in a sonicated aqueous suspension at room temperature using a Varian Cary Eclipse fluorescence spectrophotometer with a sweep analysis in the range of 400–600 nm and an excitation wavelength of 375 nm at high voltage.

2.3. Photocatalytic activity tests

The photoactivity of the CdS-M samples was determined using a closed Pyrex glass reactor (247 mL) at ambient temperature and filled with Ar atmosphere. 50 mg of CdS-M photocatalyst, in a powder form, was magnetically stirred in 150 mL of an aqueous solution containing 0.05 M Na_2S and 0.02 M Na_2SO_3 as sacrificial electron donor agents. The photocatalytic hydrogen production was determined according to the reactions that take place, and are described below:

$$CdS \xrightarrow{h} e^-(CB) + h^+(VB)$$

$$2H_2O \xrightarrow{2e^-(CB)} H_2 + 2OH^-$$

$$SO_3^{2-} + H_2O \xrightarrow{2h^+(VB)} SO_4^{2-} + 2H^+$$

$$2S^{2-} \xrightarrow{2h^+(VB)} S_2^{2-}$$

$$S_2^{2-} + SO_3^{2-} \quad S \quad {}_2O_3^{2-} + S^{2-}$$

$$SO_3^{2-} + S^{2-} \xrightarrow{2h^+(VB)} S_2O_3^{2-}$$

The closed pyrex reactor system was irradiated with a Xenon arc lamp (150W, ozone Free, LOT Oriel GmbH & CO KG, Darmstadt, Germany) for 5 h. Gas samples were extracted from the reactor every 60 min to quantify the hydrogen production by gas chromatography (Star 3400 CX chromatograph, Varian) equipped with a TCD detector and a 5 Å molecular sieve packed column using Ar as the carrier gas.

3. Results and discussion

3.1. Physicochemical characterization

3.1.1. Chemical and textural analysis

Table 1 shows the chemical composition of the CdS-M photocatalysts analysed by TXRF. The concentration of In or Ga in the mono-substituted CdS-M samples was, in both cases, lower than their nominal values which implies some losses during the synthesis. In the case of co-substituted CdS-M samples, the concentration of Ag decreased considerably with respect to the nominal value, while the concentration of In and Ga maintained the low values already observed on the monosubstituted counterparts. The atomic (Cd + M)/S ratio was similar in all CdS-M photocatalyts and was not substantially modified with respect to the value observed in the unmodified CdS reference.

The N_2 adsorption-desorption isotherms and the corresponding pore distribution of CdS-M photocatalysts are shown in Fig. 1a and b respectively. Fig. 1a shows that the isotherms of all the CdS-M samples are of type IV, which is typical of mesoporous materials, with hysteresis loops of type H3 associated with aggregates of platelet like particles forming slit-like pores. The pore sizes of the CdS-M samples (Fig. 1b) show a wide distribution in all samples with some differences in the maximum pore diameter from 15 nm in the case of the CdS-In to 35 nm in the case of the CdS-AgIn sample. All CdS-M photocatalysts showed a lower pore size than that observed on the unsubstituted CdS reference sample. The changes in the pore distribution of the CdS-M photocatalysts are derived from the differences in the degree of aggregation of the primary CdS-M particles because these particles do not develop microporosity (Fig. 1a). The textural data i.e. the BET surface area and pore size, of the CdS-M photocatalysts determined from the N_2 adsorption-desorption isotherms are shown in Table 2. The results in this table corroborate the observation that the specific surface area of the CdS was substantially modified when Ag^{+}, In^{3+} and Ga^{3+} were added to the CdS. For the mono-substituted CdS series, the In- and Ga-CdS samples showed a significant increase in their surface areas with respect to the CdS reference sample. The surface areas of the co-substituted photocatalysts decreased considerably with respect to the monosubtituted In- and Ga- counterparts. This indicates the impact of the presence of Ag on the development of the porous structure in the co-substituted CdS-M samples.

3.1.2. Powder X-Ray diffraction

Fig. 2 shows the X-ray diffraction patterns of the CdS-M photocatalysts, and Table 3 summarizes the quantification of the relative intensities of the main diffraction peaks and the calculation of the crystallite domain sizes by applying the Debye-Scherrer equation. The XRD diffraction patterns of all CdS-M photocatalysts (Fig. 2) are consistent with the reflections corresponding to the crystalline hexagonal phase of CdS (JCPDS: 01-077-2306). The low relative (001)/(002) peak intensities observed in the difractograms of all the CdS-M samples (Table 3) indicated a preferential growth along the <002> direction which is characteristic of the presence of

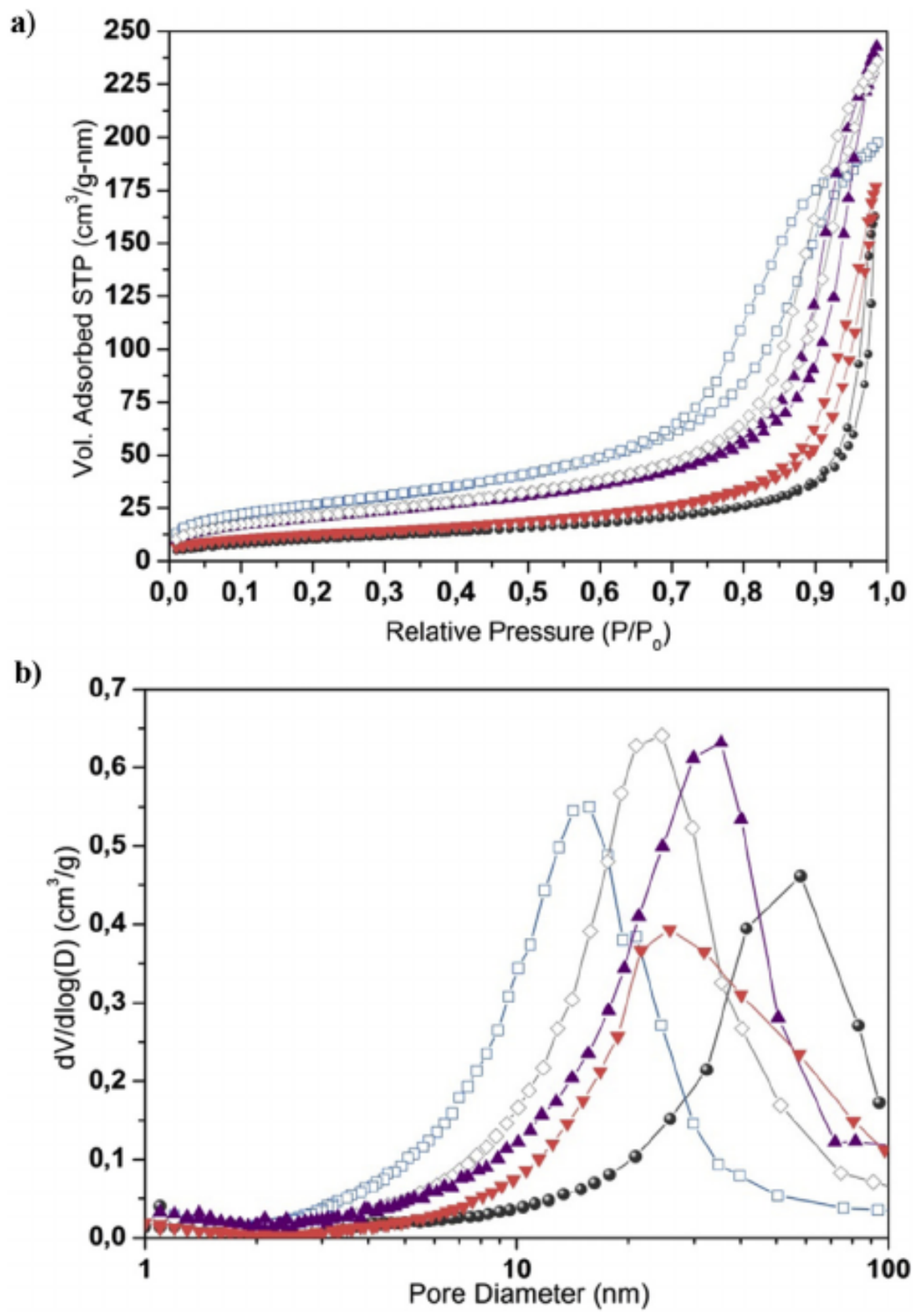

Fig. 1. N_2 adsorption-desorption isotherms (a) and pore-size distribution curves (b) of CdS-M photocatalysts; ( ) CdS-In; ( ) CdS-Ga; ( ) CdS-AgIn; ( ) CdS-AgGa and ( ) CdS (reference).

one-dimensional (1D) CdS nanostructures. The XRD profiles show that the addition of the aliovalent cations to CdS caused slight modifications to the structure and crystallite domain size with respect to the non-substituted CdS reference sample. The CdS-In and CdS-Ga photocatalysts show a pronounced decrease in both the intensity and the broadening of the (001) and (101) diffraction peaks of the CdS phase with respect to the reference sample, which is evidence of a lower development and size of the 1D nanostructures of CdS i.e. 90.9 nm for the CdS reference sample, 35.3 nm for CdS-In, and 42.4 for CdS-Ga (Table 3). In the CdS-In sample the diffraction peaks of the CdS phase show a slight shift which could indicate the replacement of the Cd^{2+} by the In^{3+} ions. The similar radii of the In^{3+} and Cd^{2+} ions explains the minimal disturbance in the CdS crystal lattice in the case of their mutual substitution. Diffraction peaks corresponding to either the In_2S_3 or $CdIn_2S_4$ phases were not observed in the XRD profile of the CdS-In which

Table 1
Chemical surface composition (atomic percentage) of CdS-M photocatalysts determined by TXRF analyses.

	Cd (at %)	S (at %)	Ag (at %)	In (at%)	Ga (at %)	(Cd + M)/S
CdS	47.4	52.6	–	–	–	0.90
CdS-In	45.5	52.9	–	1.6	–	0.89
CdS-Ga	46.1	52.4	–	–	1.5	0.91
CdS-AgIn	44.1	53.2	0.8	1.9	–	0.88
CdS-AgGa	46.0	52.4	0.4	–	1.2	0.91

Table 2
BET specific surface area, average pore diameter and pore volume of CdS-M photocatalysts determined from N_2 isotherms.

	BET m^2/g	Average Pore Diameter nm
CdS	38.6	58
CdS-In	95.2	15
CdS-Ga	78.5	25
CdS-AgIn	74.8	35
CdS-AgGa	46.3	26

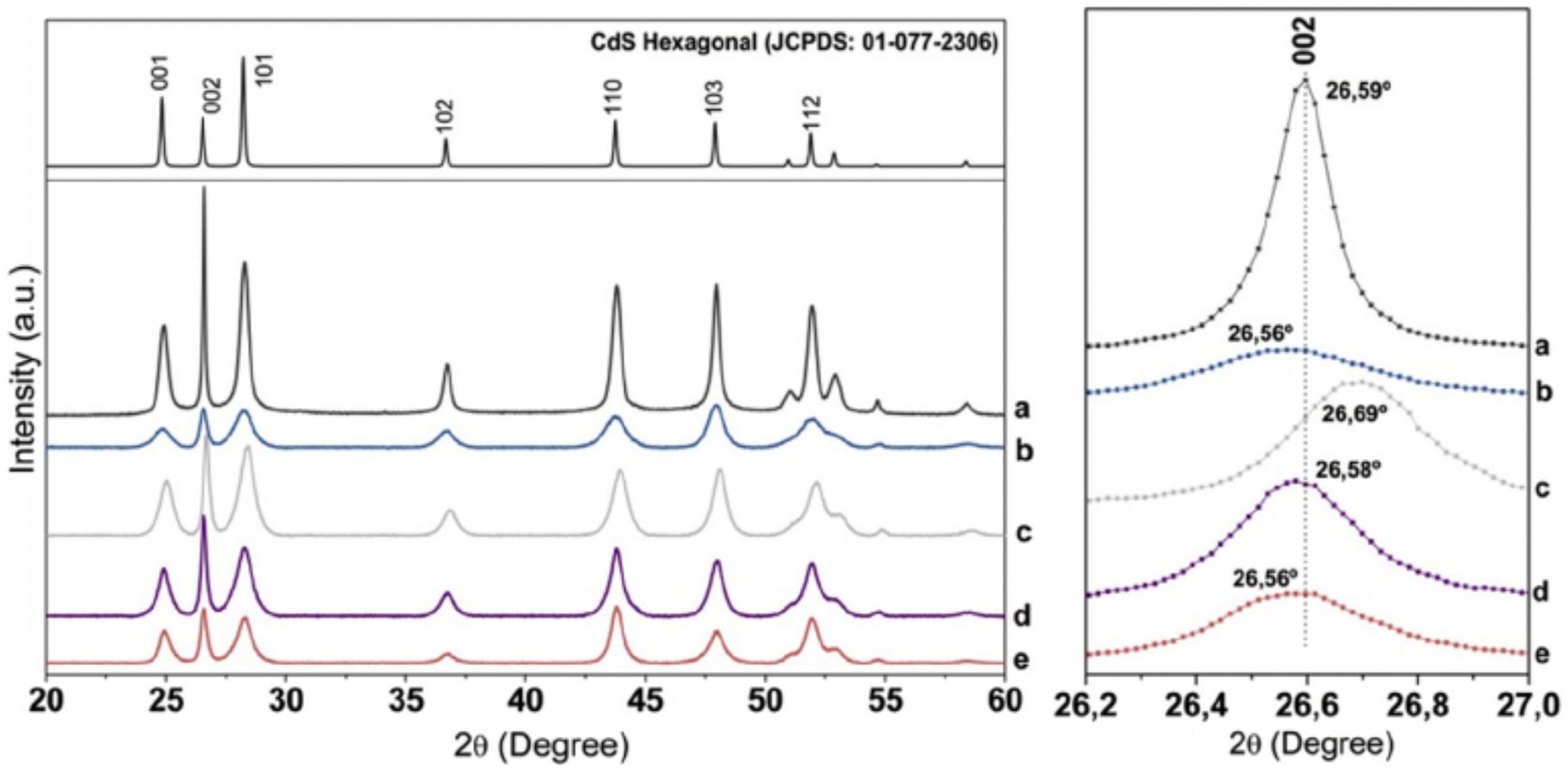

Fig. 2. XRD patterns of CdS-M photocatalysts: a) CdS (reference); b) CdS-In; c) CdS-Ga; d)CdS-AgIn and e) CdS-AgGa.

Table 3
Crystalline data of the CdS hexagonal phase detected on CdS-M photocatalysts determined from XRD data.

	Dp (nm)	Relative Intensities	microstrain
	002	$I_{(100)/(002)}$	
CdS	90.9	0.43	−0.0014
CdS-In	35.3	0.49	−0.0022
CdS-Ga	42.4	0.55	−0.0022
CdS-AgIn	42.6	0.47	−0.0018
CdS-AgGa	35.3	0.60	−0.0016

indicates a low concentration of the In segregated species and also supports the insertion of the In^{3+} ions into the CdS phase. The diffraction peaks corresponding to the CdS phase in the CdS-Ga photocatalyst show a clear shift in their position to higher angles. This is indicative of the substitution of Cd^{2+} by Ga^{3+} ions into the CdS lattice taking into account the low ionic size of the Ga^{3+} ions. Diffraction peaks corresponding to the segregated Ga^{0} or Ga_2S_3 phases were not observed in the XRD profile of this CdS-Ga sample which also points to the insertion of Ga^{3+} ions into the CdS phase. The substitution by Ga^{3+} observed in this sample contrasts with the study performed by Yang et al. [42] who observed interstitial doping of Ga ions into CdS leading to an increase in their lattice plane distances. The differences could be related to the different concentration of Ga used in both studies because it is known that at a low [Ga]/[Cd] ratio, Ga^{3+} ions replace Cd^{2+} ions in the lattice substitutionally while for a high [Ga]/[Cd] ratio Ga^{3+} ions start to enter the lattice both substitutionally and interstitially which causes an increase in the lattice distances.

The XRD profile of the co-substituted CdS-AgIn photocatalyst was close to that observed in the CdS-In counterpart, showing a low intensity and broadening of the diffraction peaks, but with some improvement in the development and crystallite size of the hexagonal structure of CdS with respect to the CdS-In counterpart. The diffractogram of this CdS-AgIn sample does not show any other diffraction peaks indicating the absence of segregated phases. The analysis of the position of the diffraction peaks of the CdS phase in the CdS-AgIn photocatalyst indicates a slight upshifting with respect to the CdS-In counterpart which means a small decrease in its lattice. This could be associated with the co-substitution of the Ag^{+} and In^{3+} ions into the CdS phase which facilitated the insertion of Ag^{+}. The known formation of solid solutions between $AgInS_2$ and metal sulfides with a wurtzite structure [37] could facilitate the observed co-substitution of the Ag and In ions in the CdS structure. Similarly, the XRD profile of the CdS-AgGa sample shows small diffraction peaks pointing to the low development of the hexagonal phase with respect to the monosubstituted counterparts. The CdS-AgGa sample does not show any shifting in the diffraction peaks previously observed on the CdS-Ga that may have been caused by the insertion of the Ag^{+} ions which compensate the lattice contraction observed with the insertion of the Ga^{3+} in the CdS structure. As indicated for the CdS-AgIn sample, the co-substitution of Ag^{+} and Ga^{3+} could be possible in view of the solid solution range of $AgGaS_2$ into sulphides with a wurtzite structure [36]. The absence of the segregated species in the XRD profile of the CdS-AgGa photocatalyst also supports the co-insertion of Ag^{+} and Ga^{3+} into the CdS structure.

The microstrain of all the CdS-M samples (Table 3) has been calculated through the slope of the Williamson-Hall plot linear fit (Fig. SI. 1). The negative slopes summarized in Table 3 are indicative of the strains associated to the compression of the CdS nanostructures caused by the insertion of the aliovalent cations on its lattice. The mono-substituted CdS-In and CdS-Ga samples show a compressive strain slightly higher than that observed in the CdS-reference sample. The compressive strain in the CdS-Ga sample is in line with the macro-strain expressed by a shift in the peak positions derived from the substitution of the Cd^{2+} ions by Ga^{3+} ions of a lower size. The compressive strain observed in the case of the CdS-In sample contrasts with the small downshift observed in its XRD peaks. This fact indicates the existence of nonuniform microstrains in the crystallites of CdS-In which produce a broad peak without significant macro-strain as derived from the similar position of the XRD peak [43]. The microstrain values in the co-substituted CdS-AgIn and CdS-AgGa are lower than in the case of the mono-substituted counterparts. This fact is a consequence of the presence of the balancing cation Ag^{+} which equlibrates the lattice stress observed in the mono-substituted counterparts.

3.1.3. Raman spectroscopy studies

The properties of the CdS and CdS-M photocatalysts were also analysed by Raman spectroscopy, at room temperature, using an excitation wavelength set at 532 nm. The non-doped CdS sample (Fig. 3a) at 302 cm^{-1} shows the typical fundamental longitudinal optical phonon mode (LO) of the hexagonal phase, and at 607 cm^{-1} the first-order overtone (2LO), as previously reported for CdS [44].

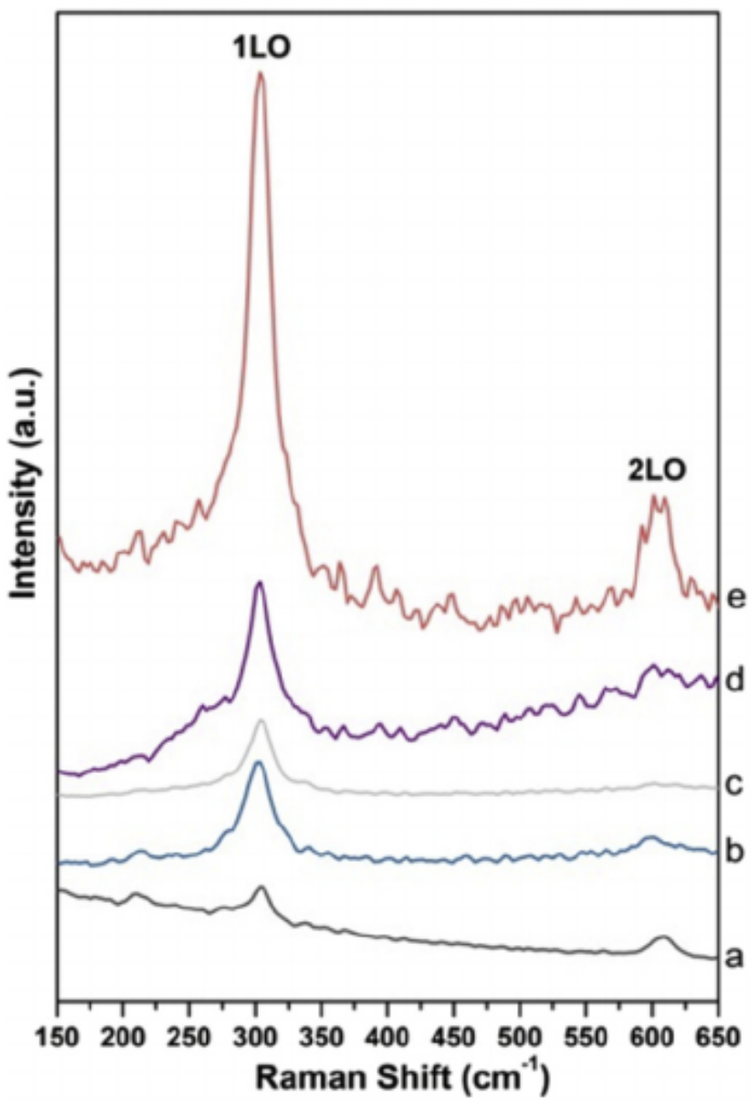

Fig. 3. Raman spectra of CdS-M photocatalysts: a) CdS (reference); b) CdS-In; c) CdS-Ga; d) CdS-AgIn and e) CdS-AgGa.

In the Raman spectra of all the doped CdS-M photocatalysts, these two spectroscopic features were still observed but with significant changes depending on the type of metal dopant. Table 4 summarizes the relevant Raman data collected from the spectroscopic measurements performed on the CdS and CdS-M samples (see Table 5).

While slight shifts have been observed in the Raman bands ascribed to the LO and 2LO modes, more pronounced changes were clearly observed in their relative intensities. The Raman data indicate a lower I_{2LO}/I_{LO} ratio for the doped samples when compared to CdS and there is a tendency for this ratio to decrease as the average diameter of the nanorods decreases. This type of observation has been reported by other authors and has been attributed to a decrease in the strength of the electron-phonon interaction occurring in nanosized CdS, to which the I_{2LO}/I_{LO} ratio is very sensitive [44–47]. However, there is a deviation in this behavior for the co-substituted CdS-AgGa and CdS-AgIn samples. These differences can arise due to the presence of residual metallic Ag [48–51]. The rise in the 1(LO) intensity could also be derived from the presence of metallic Ag nanoparticles whose electronic field interferes with the laser excitation, creating a strongly concentrated local field as consequence of the plasmon excitation on these particles. As will be discussed below, this hypothesis is supported by the XPS results that indicate the presence of metallic Ag at the surfaces of the CdS-AgIn and CdS-AgGa samples.

Table 4
Raman data collected for the CdS and CdS-M samples.

	λ (1(LO))[a]	λ (2(LO))[a]	$I_{2(LO)}/I_{1(LO)}$[a]	Width[b] (nm)
CdS	302.8 ± 0.3	607.3 ± 0.2	0.59	20
CdS-In	303.1 ± 0.9	607.1 ± 1.2	0.09	6
CdS-Ga	304.6 ± 0.3	610.8 ± 1.7	0.06	7
CdS-AgIn	303.7 ± 0.5	607.3 ± 1.9	0.22	5.8
CdS-AgGa	305.2 ± 0.9	608.4 ± 2.2	0.17	8.5

[a] Average Raman intensity values obtained from 5 Raman spectra from each sample, using the 532 nm laser source.
[b] Values taken from TEM images.

The Raman spectra discussed above were recorded in resonant conditions and therefore the bands due to the surface bound ethylenediamine, can be obscured by the intense Raman bands of the CdS. Consequently, the ATR spectra of the CdS-M photocatalysts (Fig. SI 3) show vibrational bands that have been ascribed to ethylenediamine at the CdS-M surfaces. Amine ligands at the surface of the CdS-M could have an influence on the photoactivity due to surface states that promote the transference of the photogenerated electrons. Therefore the Raman mappings over the surfaces of the CdS-M samples have also been collected. Hence, the Raman band located at 1459 cm^{-1} which is ascribed to bending the CH_2 of ethylenediamine, was monitored as the diagnosis band (Fig. SI 2). In addition, the Raman band due to the LO fundamental mode was used to monitor the CdS surface. These Raman maps were collected using 22500 spectra by raster-scanning the laser beam over a surface area of 150 × 150 μm. The integration of the absolute area underneath the band at 1495 cm^{-1} (ethylenediamine) and 305 cm^{-1} (CdS) were then used to establish the color intensity and create the Raman images shown in Fig. SI 2. The brighter colors in Fig. SI 2 center correspond to Cd. However, ethylenediamine was also detected by the few bright regions presented in Fig. SI 2 right, although with less intensity. Overall, the Raman intensities corresponding to ethylenediamine were weak regardless of the CdS-M samples analysed, and there were no significant differences between them.

3.1.4. HR-TEM analysis

The nanomorphology of the CdS-M samples was analysed by HR-TEM. The TEM image of the CdS reference sample shows well-defined nanostructures with an average size of approximately 95 nm in length and 20 nm in width, that leads to an aspect ratio of approximately 5 which is characteristic of nanorods (Fig. 4a). The lattice spacing of 0.338 nm is in accordance with the spacing of the (002) crystal plane of hexagonal CdS, which corresponds to the preferential growth direction identified by XRD (Fig. SI 4a). The CdS-In sample (Fig. 4b) has the formation of a mixture of irregular particles and nanorods with a lower development and size of 30 nm length and 6 nm width, than those observed on the CdS reference sample. The measured spacing of the CdS lattice in the CdS-In photocatalyst is 0.336 nm which is slightly lower than the (002) lattice of the hexagonal CdS planes determined in the CdS reference sample. The modification in the lattice parameter was in line with the minimal disturbance in the CdS crystal lattice observed by XRD. The presence of other segregated phases in the CdS-In sample was sparse, in line with the previous XRD analysis, with only the detection of a few domains with lattice spacing of 0.322 nm associated with the (311) plane of $CdIn_2S_4$ phase (Fig. SI 4b). The CdS-Ga sample has a nanomorphology (Fig. 5c) composed of a mixture of irregular particles and nanorods with a low extent in the formation of nanorods (28 nm in length and 7 nm width). The lattice spacing of CdS in this sample (0.321 nm) indicated some contraction in the interplanar distance of CdS corroborating the insertion of the Ga^{3+} ions as previously observed from the XRD analysis (Fig. SI 4c). TEM images of co-modified CdS-M samples (Fig. 4d and e) show a similar nanomorphology to that in the case of their mono-substituted CdS counterparts based on irregular nanoparticles and short nanorods. The CdS-AgIn showed nanostructures with an average size of 44.8 nm length and 5.8 nm width, while CdS-AgGa showed particles with 44.1 nm length and 8.5 nm width (Fig. 4d and e). The lattice spacing of the CdS phase measured on the co-substituted samples was similar to that observed on the CdS reference sample in accordance with the absence of any lattice modification derived from XRD analysis on these samples. Limited segregation of crystalline domains of $AgInS_2$ and $AgGaS_2$ was scarcely detected in the co-modified CdS-M samples (Fig. SI 4d,e).

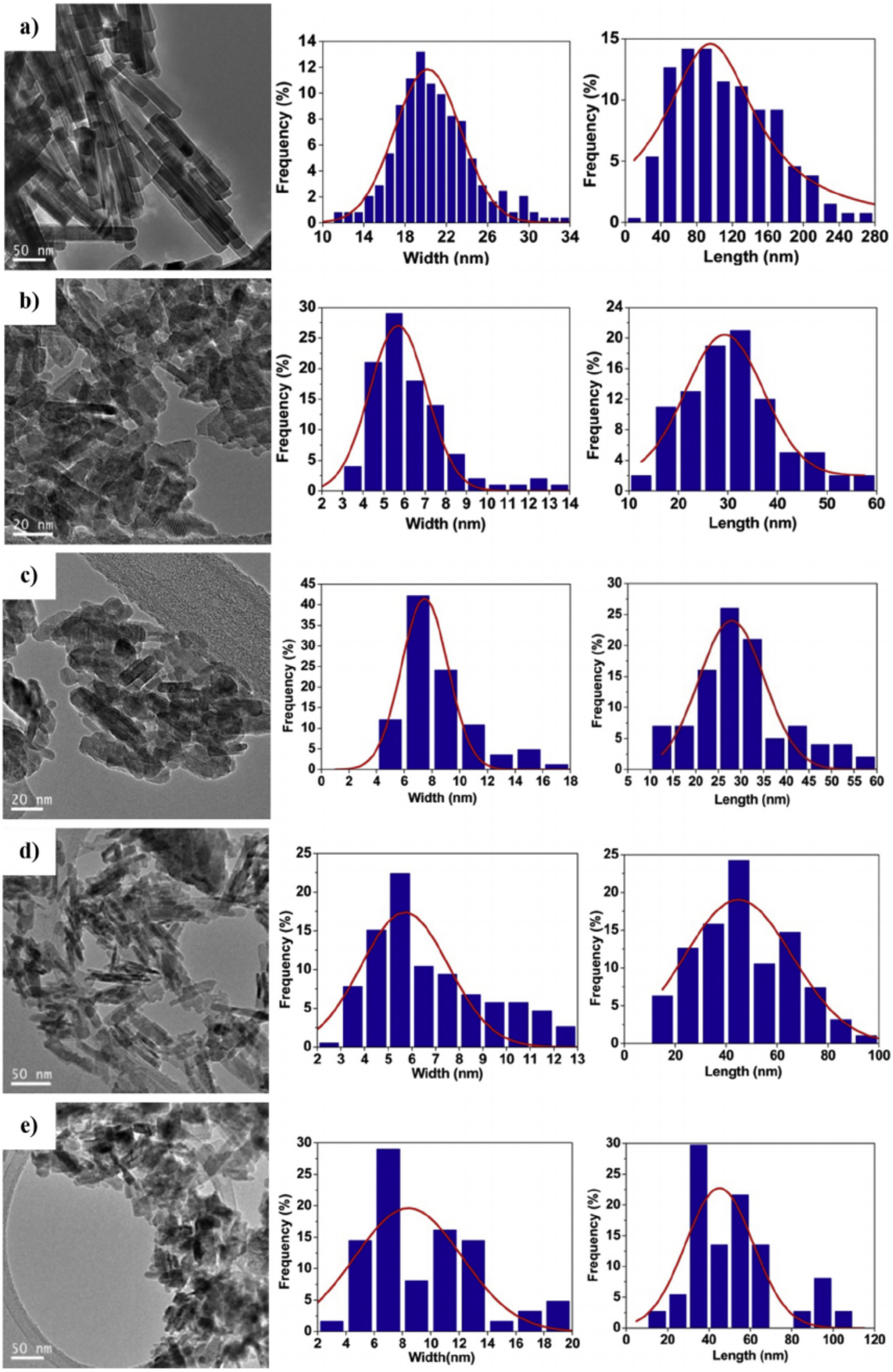

Fig. 4. HR-TEM images of CdS-M samples: (a) CdS reference, (b) CdS-In, (c) CdS-Ga, (d) CdS-AgIn and (e) CdS-AgGa.

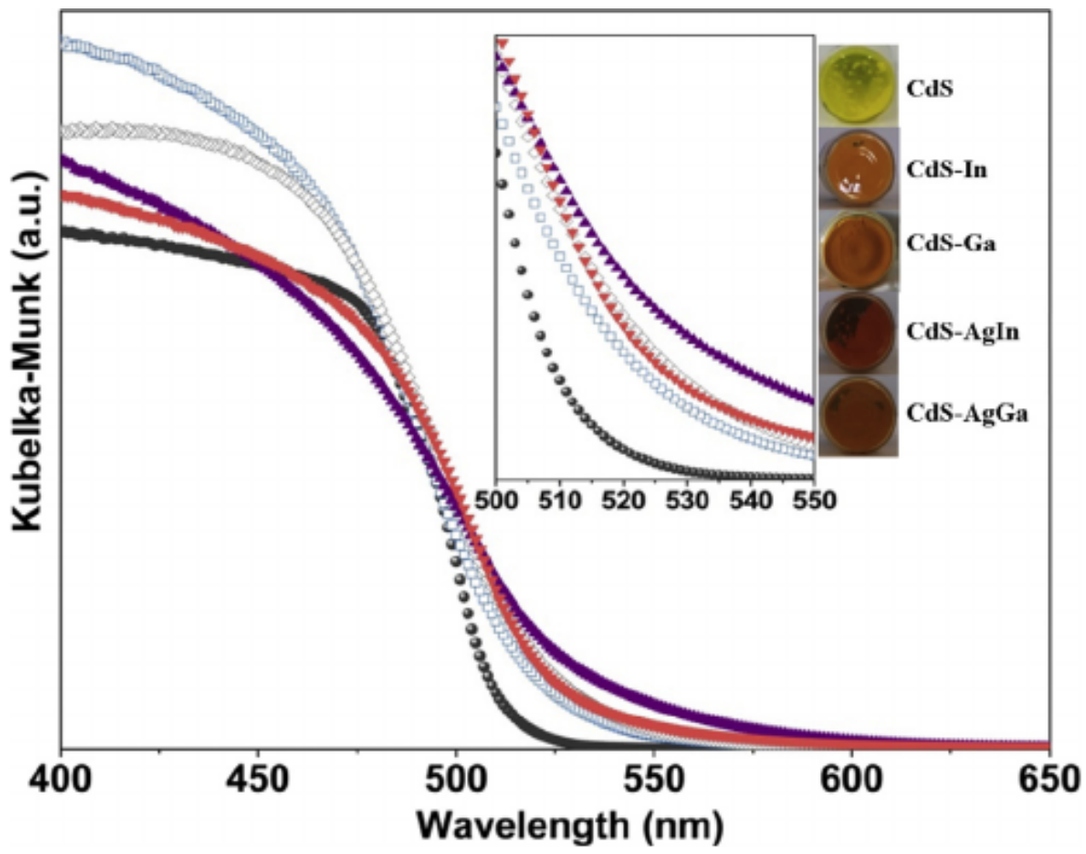

Fig. 5. UV–vis spectra of CdS-M photocatalysts: ( )CdS (reference); ( ) CdS-In; ( ) CdS-Ga; ( ) CdS-AgIn and ( ) CdS-AgGa.

3.1.5. Surface analysis by X-ray photoelectron spectroscopy

The chemical composition and state of the surface elements in the CdS-M photocalysts was investigated using X-ray photoelectron spectroscopy. The energy regions of Cd 3d, S 2p, Ga 2p and Ag 3d core-levels were recorded (Fig. SI. 5) and the binding energies are shown in Table 5. The $Cd3d_{5/2}$ level in all the CdS-M photocatalyts show a main component located at approximately 404.6 eV which is consistent with Cd^{2+} in CdS [51]. The S $2p_{3/2}$ level in all photocatalysts show a symmetric peak close to 161.0 eV which is characteristic of sulphide (S^{2-}) species [52]. The position of the main contribution in the In $3d_{5/2}$ level in the CdS-In and CdS-AgIn photocatalysts at 444.4 eV is in agreement with the presence of In^{3+} ions in a sulphide environment (In_2S_3 or $MInS_2$) [53]. A second minor component at 443.3eV was observed in the In 3d level of the CdS-In photocatalysts which is characteristics of metallic In species [44]. The binding energy for Ga $2p_{3/2}$ level in the CdS-Ga photocatalyst at 1117.6 eV is in good agreement with the reported energy values for Ga^{3+} ions [54]. A slight shift in the binding energy of the Ga $2p_{3/2}$ level was observed for the CdS-AgGa photocatalyst (1116.8 eV) that is indicative of the partial reduction of the Ga ions on the surface of this co-substituted photocatalyst [55]. The binding energy of the main peak of the Ag $3d_{5/2}$ level was 367.0–367.6 eV in the CdS-AgIn and CdS-AgGa photocatalysts which is consistent with the presence of metallic Ag particles [56]. In the CdS-AgIn photocatalysts a second minor component at 369 eV in the Ag $3d_{5/2}$ level, was also observed which could be caused by the presence of Ag particles of a smaller size. As mentioned above in the Raman confocal images, the presence of ethylenediamine over the surface of the samples has been corroborated by XPS analysis with the presence of a small hump in the region of Cd $3d_{5/2}$, corresponding to the contribution of the N 1s level.

Table 6
XPS surface composition (atomic percentage) of the CdS-M photocatalysts.

	Cd	S	In/Ga	Ag
CdS	42.7	57.3	–	–
CdS-In	41.4	55.9	2.7	–
CdS-Ga	42.6	56.7	0.7	–
CdS-AgIn	37.5	58.5	3.3	0.7
CdS-AgGa	45.2	52.4	1.8	0.6

The surface concentration of Cd, In, Ga, Ag and S calculated from the XPS intensities are listed in Table 6. The surface concentrations of In, Ga and Ag in the CdS-M samples are similar to those derived from the bulk analyses (Table 1) which indicates homogeneity of the composition of the photocatalyts, the only exception being the CdS-Ga sample for which a lower concentration of Ga content at the surface level with respect to the bulk was observed.

3.1.6. UV–vis spectra

Fig. 5 shows the UV–vis spectra of the CdS-M samples according to the Kubelka-Munk function. The CdS-M photocatalysts show one slope in their absorption edges which indicated single phase with allowed transitions. The photocatalysts show a similar absorption edge with differences in their definition and position depending on the element introduced in the CdS lattice. Shifting in the absorption edges to higher wavelengths with respect to the CdS reference sample was observed for the CdS-In, CdS-Ga, CdS-AgIn and CdS-AgGa samples. This produces a colour change in the solid photocatalysts as shown in Fig. 5 (inset). The sharpness of the adsorption profiles of the CdS-M photocatalysts increases following the sequence CdS > CdS-In > CdS-AgGa > CdS-Ga > CdS-AgIn which coincides with the variation in the crystallinity of the CdS nanostructures observed by XRD and TEM. This is in accordance with the fact that nanostructures with high crystallinity and low number of structural defects are associated with a better definition of the absorption edge [57]. The absorption capacity at a wavelength lower than 525 nm also shows differences between the CdS-M samples. An increase in the absorption capacity of the CdS-M photocatalysts corresponding to a decrease in the particle size of the CdS nanostructures was observed, which is a consequence of their higher surface being able to absorb radiation.

Defects in the CdS structures can cause a tailing effect on their spectra which are called Urbach tails [29,40]. These are due to the presence of localized electronic states near the band gap edges. The quantification of the density of the defects near the band gap of the CdS-M photocatalysts calculated using the Urbach energy parameter Eu (Fig. SI. 3) is shown in Table 7. The lower Eu value was observed in the CdS reference sample associated with the well defined electronic states of its high crystalline nanostructures. The Eu parameter in the CdS-M photocatalysts increases in parallel with the increase in their lattice defects related to the gradual lowering in crystallinity and size as derived from TEM and XRD analyses: CdS-In < CdS-Ga < CdS-AgIn < CdS-AgGa. In addition, the greater

Table 5
XPS binding energies (eV) of core electrons of the CdS-M photocatalysts.

	Cd $3d_{5/2}$	S $2p_{3/2}$	Ga $2p_{3/2}$	In $3d_{5/2}$	Ag $3d_{5/2}$
CdS	404.6	161.1	–	–	–
CdS-In	404.6	161.1	–	444.4 (81)/443.3(19)	–
CdS-Ga	404.6	161.0	1117.6	–	–
CdS-AgIn	404.7	161.3	–	444.5	367.6 (84)/369(16)
CdS-AgGa	404.6	161.0	1116.8	–	367.0

Peak percentages in parentheses.

Table 7
Band Gap energy and Urbach energy derived from UV–visible spectra of CdS-M photocatalysts.

	BG	Eu
	eV	meV
CdS	2.46	41.7
CdS-In	2.48	78.8
CdS-Ga	2.47	79.1
CdS-AgIn	2.41	113.4
CdS-AgGa	2.42	103.3

structural disorder derived from the higher Eu values could be derived from the higher structural disorder due to the Cd substitution or Cd/S vacancies which contribute to extending the band tail.

The band gap values of the CdS-M photocatalysts were calculated from the slope of the Tauc plot (Fig. 6) and are shown in Table 7. The CdS-In and CdS-Ga samples show a slight increase in the band gap with respect to the CdS reference sample. This increase in the band gap could be a consequence of the Burstein–Moss effect associated with the increase in the carrier concentration from the substitution of Cd^{2+} by the In^{3+} or Ga^{3+} ions [58,59]. Conversely, the co-substituted photocatalysts, CdS-AgIn and CdS-AgGa, show a significant narrowing in their band gap with respect to the CdS reference sample. The change in the band gap demonstrates the co-substitution of the Ag^{+} and In^{3+}/Ga^{3+} ions into the CdS phase because it is known that the insertion of cations in the CdS lattice promotes the appearance of localized states near the bandgap region, as described above using an analysis of the Urbach tails. This favours the promotion of the electrons

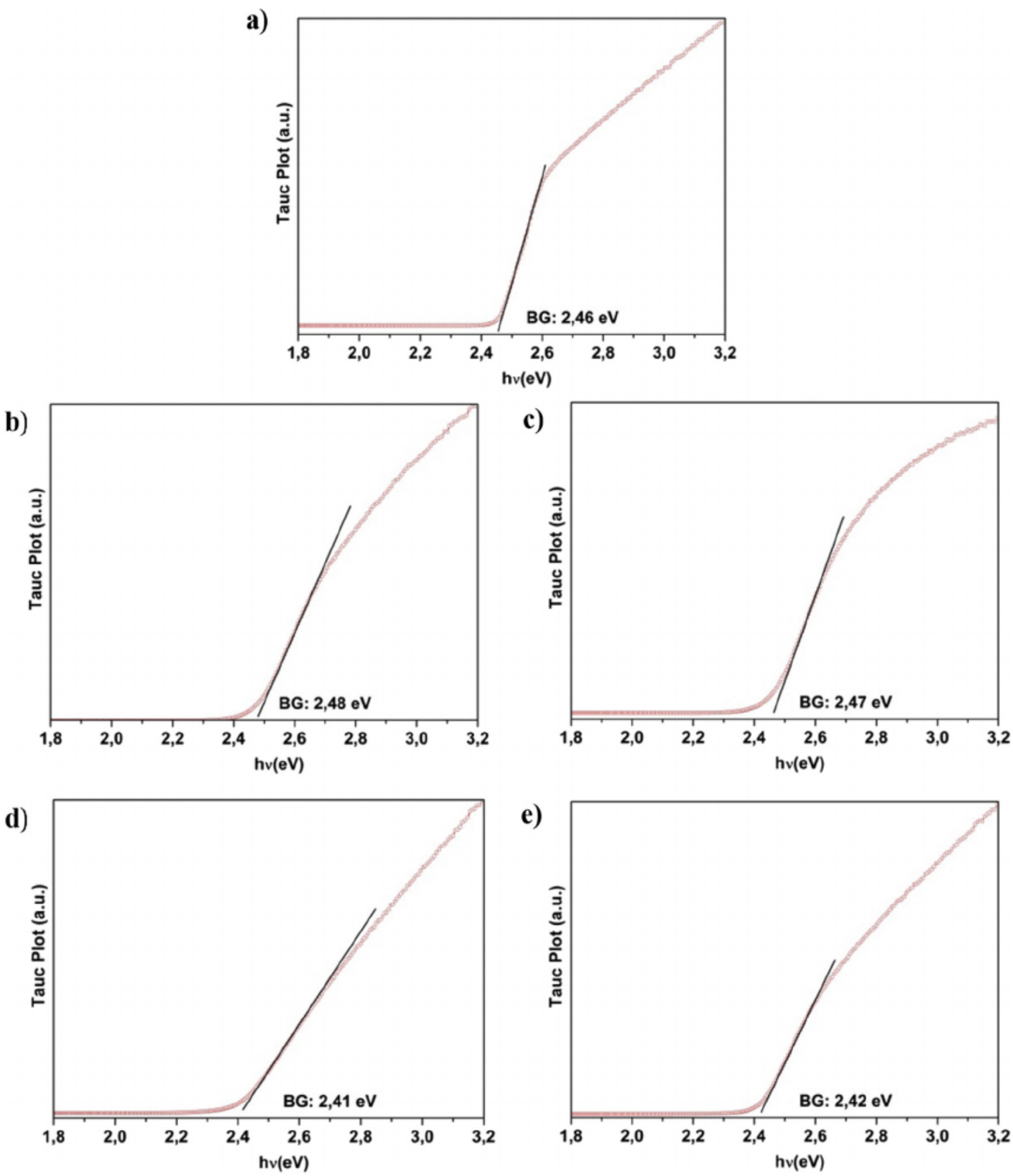

Fig. 6. Tauc plots of CdS-M photocatalysts: a) CdS (reference); b) CdS-In; c) CdS-Ga; d) CdS-AgIn and e) CdS-AgGa.

from the conduction band to the tail, and tail to tail transitions [60]. The observed decrease in the band gap for the CdS-AgIn photocatalyst concurs with the work of Zang *et al* [61] who associated the narrowing in the band gap with the downward and upward shifts in the conduction and the valence bands of the CdS from the contribution of the In and Ag states inserted into the CdS structure i.e. the top edge of Ev by hybridization of the Ag 4d and S 3p orbitals, and the bottom edge of Ec by hybridization of the In5s5p and Cd5s5p. In the case of the CdS-AgGa photocatalyst there are no references in the literature to the formation and electronic structure of ternary CdS-Ag-Ga systems with the insertion of Ag and Ga. Nevertheless, taking into account the valence electron energies of the Cd, Ag and Ga elements [62] it can be assumed that the conduction band of the CdS-AgGa photocatalyst was composed of hybrid orbitals of Cd 5s5p and Ga 4p4d, and the valence band comprised of S 3p and Ag 4d orbitals.

3.1.7. Ultraviolet photoelectron spectroscopy (UPS)

UPS was used to determine the relative position of the valence band maximum energy (VBM) with respect to the conduction band minimum (CBM) [41]. Fig. 7 shows the magnified UPS spectra of the CdS-M samples used to deduct the energy value of E_{VBM} from the intersection of the linear portion of spectrum and the baseline. The summarized E_{VBM} and work function (Φ) derived from the UPS spectra are listed in Table 8 which shows slight differences in the position of the valence band maximum energy of the CdS-M samples.

The relative positions of E_{VBM} and E_{CBM} presented in Fig. 8 was determined using the E_{VBM} values calculated from the UPS and the optical band gap values derived from the UV–vis spectra. It is well-known that 5s5p orbitals of Cd contribute mainly to the bottom of the conduction band of CdS while the 3p orbital of S contributes to the top of the valence band of CdS [63]. Theoretical calculations of the band structure of M-doped CdS (M = Ga or AgIn) [42,61,62] indicated variations in the position of the top edge of valence bands of CdS from the hybridization of Ga 4s, Ag 4d and S 3p orbitals while the In 5s5p states mainly contribute to the bottom edge of the conduction band. Therefore, the different relative position of the E_{VBM} of CdS-Ga, CdS-AgIn and CdS-AgGa with respect to the CdS-In sample could be derived from their different hybrid band levels near the band edges i.e. S3p-Ga4s for CdS-Ga, S3p-Ag4d for CdS-AgIn, S3p-Ga4s-Ag4d for CdS-AgGa and S3p for CdS-In.

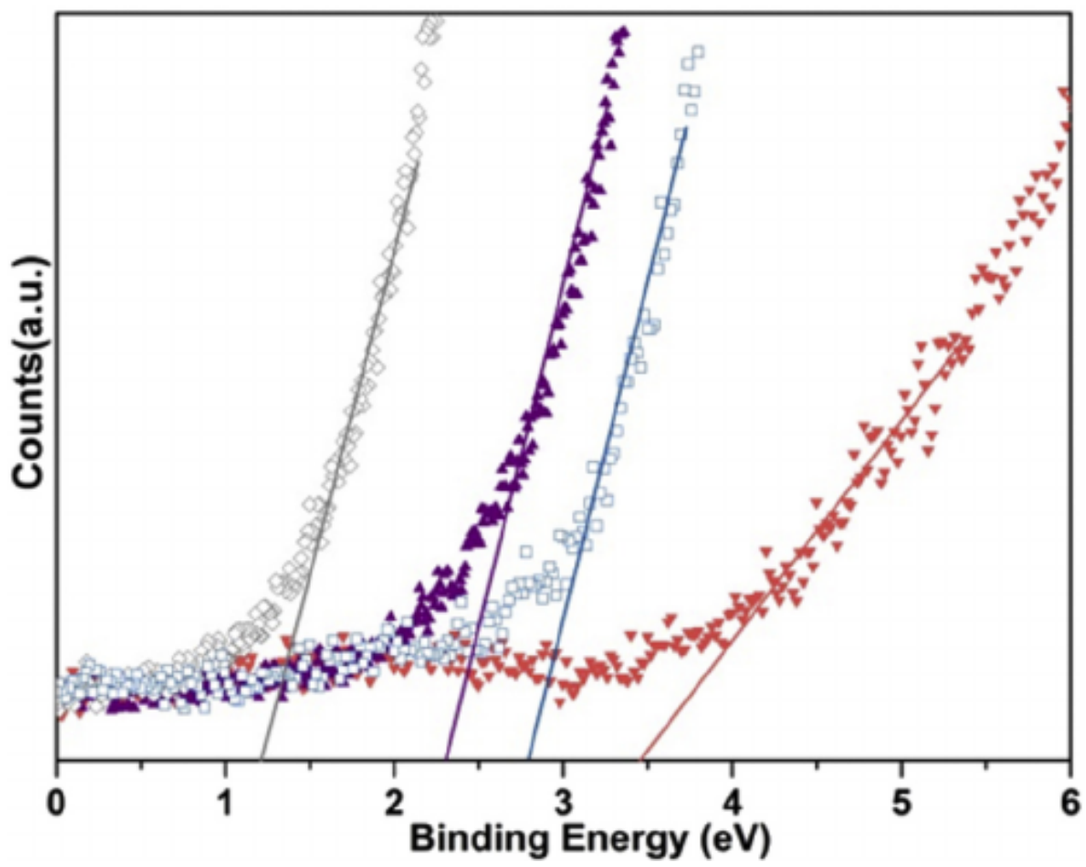

Fig. 7. UPS spectra of low-binding energy region for E_{VBM} determination ( ) CdS-In; ( ) CdS-Ga; ( ) CdS-AgIn and ( ) CdS-AgGa.

Table 8
Calculated valence band maximum energy and work function derived from UPS on CdS-M photocatalysts.

	E_{VBM} / eV	Φ / eV
CdS-In	2.92	4.2
CdS-Ga	1.24	4.2
CdS-AgIn	2.31	4.2
CdS-AgGa	3.44	4.2

3.1.8. Photoluminescence analysis (PL)

Fig. 9 shows the PL spectra of the CdS-M photocatalysts measured in an aqueous suspension at room temperature with an excitation wavelength at 375 nm. The PL spectra of the CdS reference sample photocatalyst shows a broad emission band in the 525–650 nm range. The emission band centered at ~525 nm originates from band to band transitions near the band gap of the CdS nanostructures since the peak energy of this band (2.47 eV) is closed to its bandgap [64–67]. The broad emission bands located at wavelengths higher than the 550 nm observed in the PL spectrum of the CdS reference sample are commonly related to the recombination of shallow trapped electrons in sulfur vacancy defect energy states (Vs) with holes in the valence band.

The CdS-Ga and CdS-In photocatalysts exhibited a broad PL profile similar to that observed in the CdS reference sample but with lower intensity in spite of their low particle size and less well developed crystalline structure. The lower PL intensity in the CdS-Ga and CdS-In photocatalysts can be derived from the insertion of Ga^{3+}/In^{3+} ions into the CdS lattice which creates levels that can compensate for the higher recombination rate of electrons and holes expected from their the low particle size and crystallinity. This observation was consistent with the results in the literature indicating the quenching effect of the luminescence of CdS when indium was introduced in its structure [68]. In the case of the CdS-In photocatalyst the presence of the surface metallic In species detected by XPS, which introduces deep levels, could also contribute to the decrease in the PL emission of this sample with respect to the CdS reference sample. The co-substituted CdS-AgIn and CdS-AgGa photocatalysts show a clear decrease and shifting to higher wavelengths in the their PL emission spectra with respect to CdS-In and CdS-Ga counterparts. The shifting of the PL to the higher wavelengths observed for the co-substituted photocatalysts is consistent with band to band transitions near the band gap since their peak energies are close to the band gap derived from UV–vis analysis. The quenching in the PL of the co-substituted photocatalysts may be derived from the presence of segregated metallic silver as detected by XPS, which could also favour the spatial separation of photogenerated charges via new nonradiative pathways created by the proximity of the metal resulting from the electron transfer from CdS to the metallic particles [69].

3.2. Structure and photoactivity

As illustrated in Fig. 10 there are evident differences in the photoactivity of the CdS-M samples. The inclusion of Ga- or In- on the CdS structure provokes a substantial decrease in the photoactivity of the photocatalyts with respect to the CdS reference. The co-substitution with Ag and In also produces a very low H_2 production rate with similar values to that obtained on the sample replaced solely with indium. Only the co-substituted CdS-AgGa photocatalyst showed an improvement in the photoproduction of hydrogen with respect to the CdS reference sample.

Physicochemical characterization of the CdS-M photocatalysts has shown the effectiveness of the solvothermal synthesis for the insertion of Ga^{3+}, In^{3+}, Ga^{3+}/Ag^{+} and In^{3+}/Ag^{+} into the hexagonal

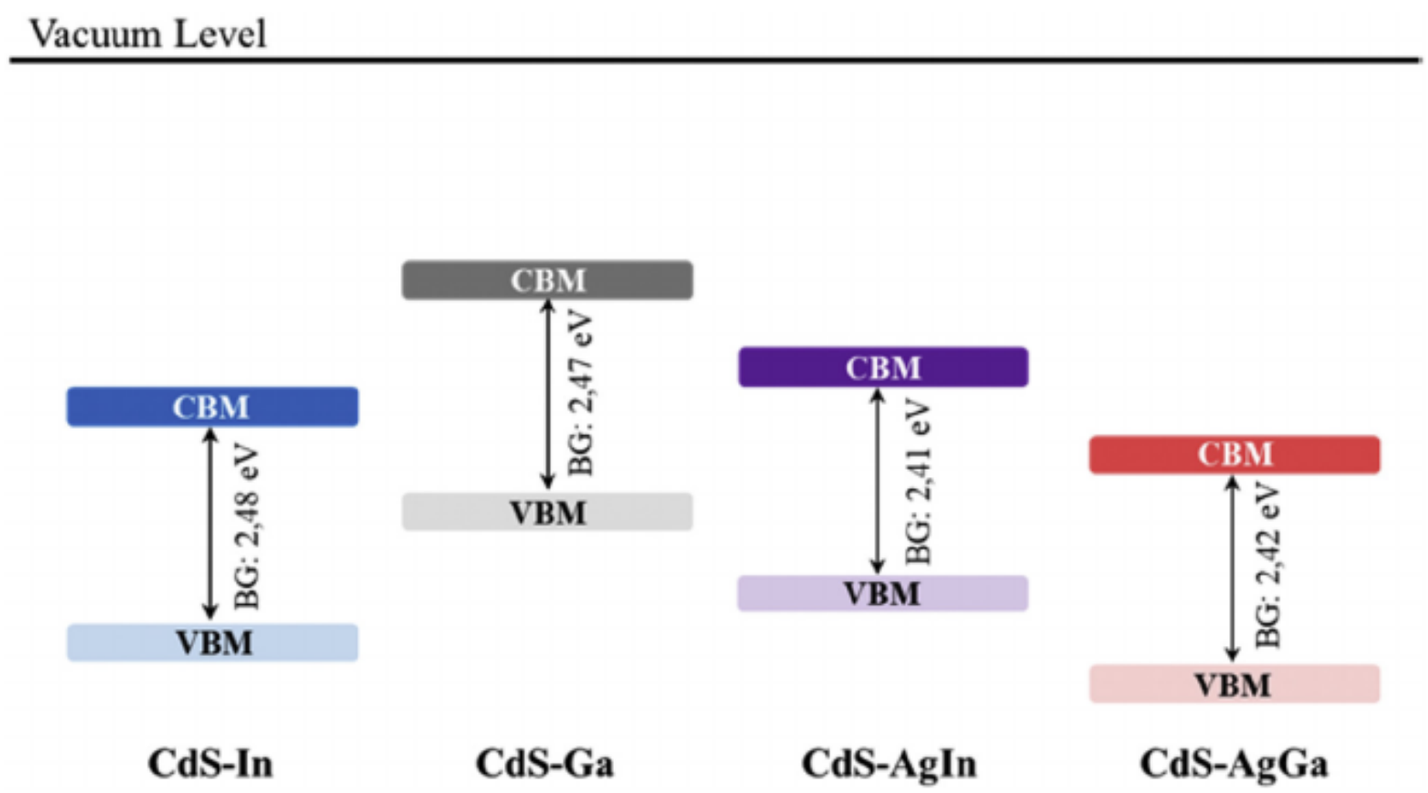

Fig. 8. Schematic diagram displaying the relative positions of VBM and CBM obtained from the UPS and UV–vis for CdS-M samples.

crystal lattice of one-dimensional CdS nanostructures with low concentration of segregrated species. The solvothermal formation of nanocrystals of CdS-M samples using ethylenediamine (EDA) as a solvent and elemental sulfur includes the following steps [7,8]:

(1) formation of Cd^{2+} and M^{n+} complexes with EDA (Cd-EDA and M-EDA),

$$Cd^{2+} + 2\ EDA \quad [M(EDA)\ _2]^{2+} \tag{1}$$

$$M^{n+} + x\ EDA \quad [M(EDA)\ _x]^{n+}$$

(2) reaction of elemental sulfur with EDA to form S^{2-}, S_6^{2-}, S_4^- and other polyanions [24,70]

$$S + EDA \quad S^{2-} \tag{2}$$

(3) reaction of M-EDA and Cd-EDA complexes with S^{2-} ions to form crystalline CdS-M structures. On the basis of the large difference in the solubility product constants of the individual sulfides the segregation of M- and Cd-sulfides as intermediates is expected

$$[Cd(EDA)_2]^{2+} + S^{2-} \quad CdS + 2\ EDA \tag{3}$$

$$[M(EDA)_x]^{n+} + n/2\ S^{2-} \quad MS\ _{n/2} + x\ EDA$$

and,

(4) finally the formation of the mixed CdS-M sulfides from the M- and Cd-sulfides as indicated in the literature concerning the solvothermal synthesis of mixed sulphides [71,72]:

$$CdS + MS_{n/2} \quad CdS{-}M \tag{4}$$

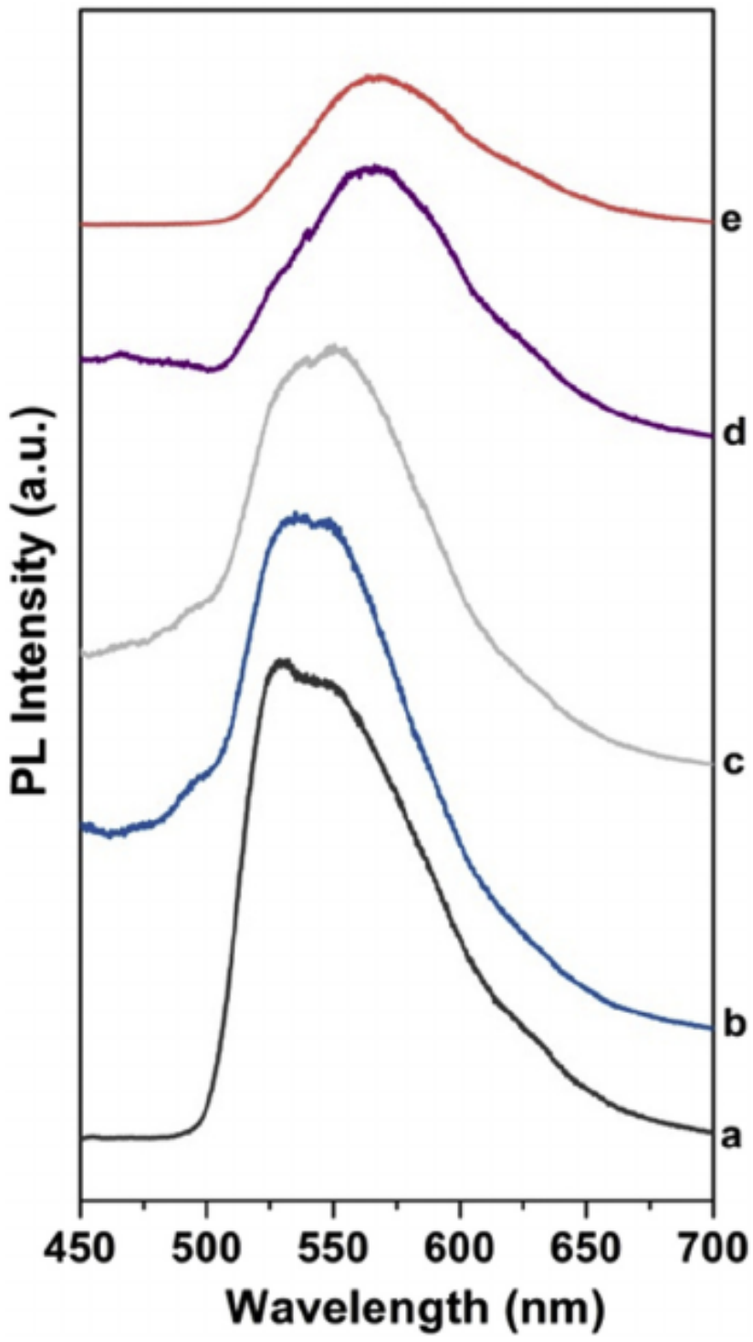

Fig. 9. PL spectra of CdS-M photocatalysts (375 nm excitation wavelength): a) CdS (reference) b) CdS-In; c) CdS-Ga; d) CdS-AgIn and e) CdS-AgGa.

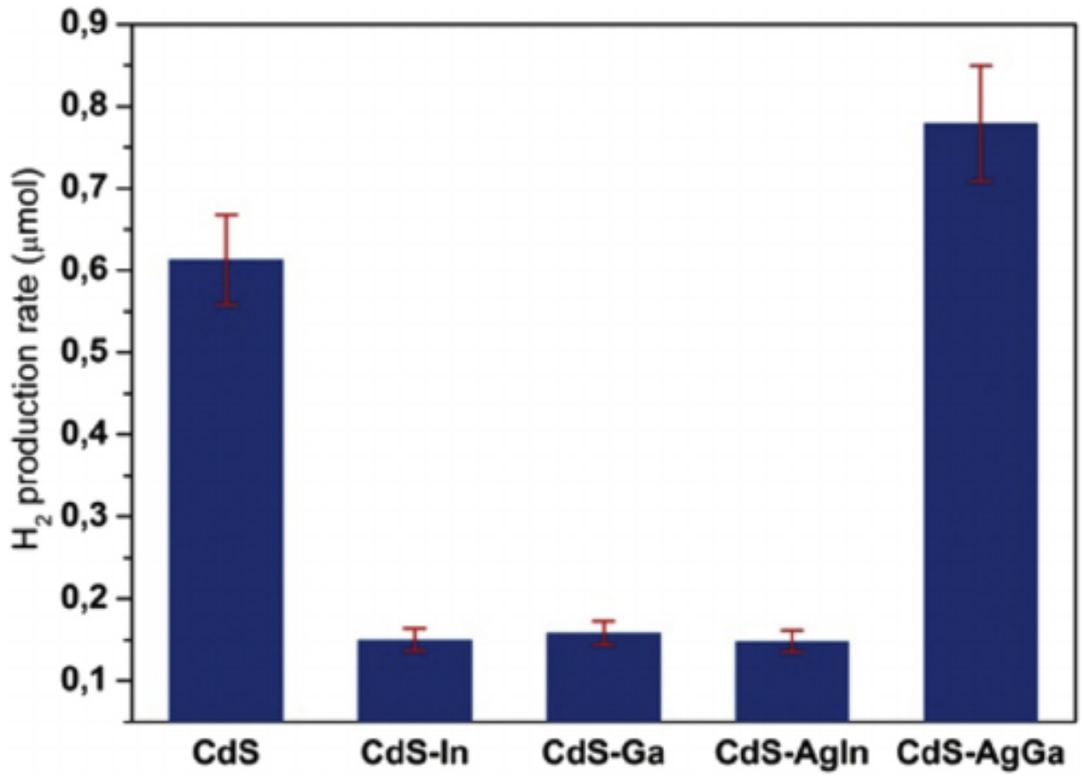

Fig. 10. Hydrogen evolution rate (μmol) and standard deviation on CdS-*M* photocatalysts.

From the formation mechanism mentioned above, one can see that the development and size of the nanostructures of the CdS-M samples is controlled by the kinetics of the nucleation of the individual sulfides and the growth of the mixed CdS-M sulfide which are determined by the release rate of S^{2-} ions as well as the relative stability of the $[M(EDA)_x]^{n+}$ complexes with respect to the formation of the sulphide precipitates. The slow release of S^{2-} ions favours a low rate of nucleation and growth, leading to the formation of nanostructures of low crystallinity and size. Therefore, the low solubility of the In- and Ga- sulfides ($In_2S_3 < Ga_2S_3 <$ CdS) favours the formation of small In_2S_3 and Ga_2S_3 nuclei. These nuclei could act as nucleating platforms which probably modify the normal growth of the CdS nanostructures observed in the CdS reference sample, and justifies the lower size and crystallinity observed for the mixed CdS-In and CdS-Ga sulphides when compared with the CdS reference. When In^{3+} or Ga^{3+} ions were simultaneously combined with Ag^{+} the growth of CdS was also modified, in this case by the initial formation of small nuclei of AgIn or GaIn sulfides. The low size of the crystalline phase observed in the mixed CdS-AgGa sulfide could be derived from the initial formation of small AgGa sulfide nuclei, taking into account its low solubility, which could prevent the growth of the CdS nanostructures and limit the growth of the mixed sulfides.

The differences in the photoactivity of the CdS-M samples should be analyzed taking into account their structural and photo-physical properties because these factors govern the photocatalytic steps involved in the production of hydrogen: light absorption to generate the charge carriers (electrons and holes), and the migration and reaction of these charge carriers to the surface, to produce the redox reactions [2]. The generation of the charge carriers is governed by the photo-physical properties of the CdS-M photocatalysts. The analysis of the light absorption capacity of photocalysts from the UV–vis analyses (Fig. 5) showed modifications in the visible light absorption capacity of the CdS-M photocatalysts through the modification in their band gap and absorbance at wavelengths lower than 525 nm. The production rate of the CdS-M photocatalysts in Fig. 11 are normalized per surface area ($\mu mol/h^{-1}\cdot m^2\cdot cat$) in order to understand the photoactivity trends of the photocatalysts associated with their electronic/structural bulk changes because as previously shown in the textural analysis, they undergo significant changes in the surface area. The comparison between the bandgap of the CdS-M samples with their photoactivity for hydrogen evolution indicated that there is no parallel behaviour between both parameters (Fig. 11). The CdS-AgGa photocatalyst is the only sample that shows higher photoactivity with respect to the CdS reference sample, which can be related to the enhancement in the visible light absorption of the photocatalyts with the co-insertion of Ag and Ga in the CdS structure. Conversely, the CdS-Ga and CdS-In photocatalysts show a slight increase in their band gap which reduces their capacity for visible light absorption. The increase in the band gap observed for CdS-In and CdS-Ga samples is due to the band filling i.e. the Burstein-Moss effect, because the high doping density in these samples leads to degenerate semiconductors in which the Fermi level shifts to a higher energy with respect to the bottom of the conduction band. This would explain the increase in the band gap and their lower photoactivity with respect to the CdS reference sample. The drop in photoactivity of the CdS-AgIn was not expected taking into account their improvement for the visible light absorption associated with the decrease in band gap. Therefore, other explanations besides the variation in the capacity for visible light absorption should be explored in order to justify the drop in activity observed on the CdS-AgIn photocatalyst.

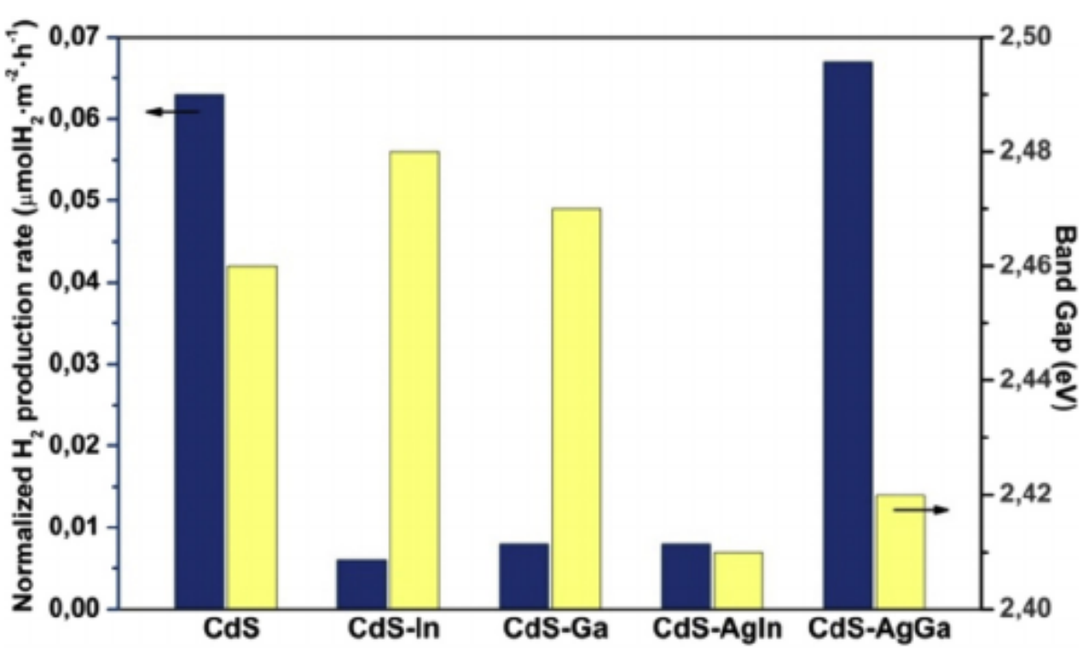

Fig. 11. Relationship between surface-normalized hydrogen evolution rate ($\mu mol/m^2\cdot h$) and band gap of the CdS-M samples.

In addition to the generation of the charge carriers, related to the optical band-gap, the mobility and use of the charge carriers i.e. electron and holes, are other factors that should be discussed in the analysis of the relationship between the photoactivity and the structure of the CdS-M photocatalysts. The high mobility, the low rate of recombination and the high efficiency in the transfer of the charge carriers to the surface molecules results in an improvement in the photocatalytic H_2 production rates. The efficiency in the separation of charge-carriers is related to the number of structural defects; the size and presence of co-catalysts on the surface of the CdS-M photocatalysts. A decrease in the rate of the recombination processes is associated with photocatalysts structures which exhibit well developed crystallinity, a low number of structural defects and the presence of co-catalysts. The PL spectra of CdS-Ga and CdS-In photocatalysts (Fig. 9) show a slightly lower charge-carrier recombination processes on these samples with respect to the CdS reference sample. Therefore the possible contribution of the recombination processes associated with the substitution of Ga or In, on the CdS structure could be discarded as a cause for the low photoactivity observed on these samples. The same argument applies to the CdS-AgIn sample which shows low photoactivity in spite of a clear decrease in the PL emission associated with the low rate in the charge-carrier recombination processes derived from the presence of segregated silver which favours the spatial separation of photogenerated charges.

The reaction of charge carriers i.e. the electron and holes, on the photocatalyst surface is the last factor to take into consideration in the analysis of the photoactivity of the CdS-M samples. It is well-known that the potential of the photogenerated electrons and holes to be able to react depends on the relative energy of the conduction band and the valence band levels with respect to the potential to produce the redox reactions involved in the final production of H_2.·As deduced from the relative band structure of the CdS-M samples illustrated in Fig. 8, the CdS-In, CdS-Ga and CdS-AgIn samples show an upshift in the relative position of the valence band energy with respect to the CdS-AgGa counterpart, which coincides with the decrease in the H_2 production rate observed in the former. Therefore, the upward shift in the top edge of the valence band observed in the CdS-In, CdS-Ga and CdS-AgIn samples could also justify their low photoactivity by a decrease in the driving force for the oxidation of S^{2-}/SO_3^{2-} species.

The characterization of CdS-AgIn and CdS-AgGa samples by XPS showed the presence of small amounts of metallic Ag

nanoparticles. These species can act as co-catalysts improving the efficiency of photocatalysts as a result of transferring the electrons to surface molecules thus reducing the activation energy for the hydrogen production [73,74]. Therefore, part of the improvement in the photoactivity observed in the CdS-AgGa sample, could also be derived from the existence of metallic silver at the surface which facilitates the electron transfer reaction and promotes the photocatalytic hydrogen production.

The co-addition of Ag^{+}-In^{3+} and Ag^{+}-Ga^{3+} favours the insertion of Ag^{+} ions into the CdS lattice. Among the co-substituted photocatalysts, only the CdS-AgGa showed a higher photoactivity with respect to the CdS. It is the first time that the ternary sulfide CdS-AgGa photocatalyst has been synthesized and reported as an active photocatalyst under a visible light opening a new way to tune the photocatalytic properties of CdS by co-doping with Ag^{+} and Ga^{3+}. Obviously, the photocatalyst CdS-AgGa has not yet been optimized as it needs further improvements in its photocatalytic activity by controlling the doping content and the optimization of the solvothermal variables.

4. Conclusions

Solvothermal synthesis of CdS-M photocatalysts has been succesful for the insertion of Ga^{3+}, In^{3+}, Ga^{3+}/Ag^{+} and In^{3+}/Ag^{+} into the hexagonal crystal lattice of one-dimensional CdS nanostructures with a low concentration of segregrated species. UV–vis analyses showed modifications in the visible light absorption capacity of the CdS-M photocatalysts through the modification in their band gap and absorbance at wavelengths lower than 525 nm. The insertion of In^{3+} or Ga^{3+} in the CdS leads to an increase in its band gap, while the co-addition of Ag^{+}-In^{3+} and Ag^{+}-Ga^{3+} favours the insertion of Ag^{+} into the CdS lattice forming $Ag(In/Ga)_xCd_{1-x}S$ solid solutions with a lower band gap. The relative position of E_{VBM} also varies with the insertion of Ga^{3+}, In^{3+}, Ga^{3+}/Ag^{+} and In^{3+}/Ag^{+} into the CdS lattice. The CdS-In, CdS-Ga and CdS-AgIn samples show an upshift in the relative position of the valence band energy with respect to the CdS-AgGa counterpart. The upward shift in the top edge of the valence band observed in the CdS-In, CdS-Ga and CdS-AgIn samples could justify their low photoactivity by a decrease in the driving force for the oxidation of S^{2-}/SO_3^{2-} species. The CdS-AgGa photocatalyst shows a higher photoactivity related to the band gap narrowing and downshift in the relative position of the valence band energy which enhances both their visible light absorption, and the potential for oxidation, respectively. Solvothermal synthesis the CdS-AgGa photocatalyst produces a small segregation of metallic Ag nanoparticles at the surface which also assist in the photoactivity of the sample. In the case of the CdS-AgGa photocatalyst, this is the first time that this ternary sulfide has been synthesized and reported as photocatalyst active under a visible light opening a new way to tune the photocatalytic properties of CdS by co-doping with Ag^{+} and Ga^{3+}.

Acknowledgements

The present work was performed within the research program supported by MINECO (Spain) under the project CTQ2016-76505-C3-1-R and CAM within the S2013/MAE-288 project. E. Soto would like to acknowledge MINECO for the FPI research grants.

Appendix A. Supplementary data

Supplementary data related to this article can be found at https://doi.org/10.1016/j.mtener.2018.06.009.

References

[1] A. Kudo, Development of photocatalysts materials for water splitting with the aim at photon energy conversion, J. Cer. Soc. Japan 109 (2001) S81–S88.
[2] A. Kudo, Y. Miseki, Heterogeneous photocatalyst materials for water splitting, Chem. Soc. Rev. 38 (1) (2009) 253–278.
[3] H. Ahmad, S.K. Kamarudin, L.J. Minggu, M. Kassim, Hydrogen from photocatalytic water splitting process: a review, Renew. Sust. Energ. Rev. 43 (2015) 599–610.
[4] F.E. Osterloh, Inorganic materials as catalysts for photochemical splitting of water, Chem. Mater. 20 (2008), 35–34.
[5] J. Sabaté, S. Cervera-March, R. Simarro, J. Gimen éz, Photocatalytic production of hydrogen from sulfide and sulfite waste streams.A kinetic model for reactions occurring in illuminated suspensions of CdS, Chem. Eng. Sci. 45 (10) (1990) 3089–3096.
[6] N. Bao, L. Shen, T. Takata, K. Domen, Self templated synthesis of nanoporous CdS nanostructures for highly efficient photocatalytic hydrogen production under visible light, Chem. Mater. 20 (2008) 110–117.
[7] F. Vaquero, R.M. Navarro, J.L.G. Fierro, Influence of the solvent on the structure, morphology and performance for H_2 evolution of CdS photocatalysts prepared by solvothermal method, Appl. Catal. B Environ. 203 (2017) 753–767.
[8] F. Vaquero, R.M. Navarro, J.L.G. Fierro, Evolution of the nanostructure of CdS using solvothermal synthesis at different temperature and its influence on the photoactivity for hydrogen production, Int. J. Hydrogen Energy 41 (27) (2016) 11558–11567.
[9] F. Vaquero, J.L.G. Fierro, R.M. Navarro Yerga, From nanorods to nanowires of CdS synthesized by a solvothermal method: influence of the morphology on the photoactivity for hydrogen evolution from water, Molecules 21 (4) (2016) 401.
[10] T. Zhai, X. Fang, L. Li, Y. Bando, D. Golberg, One-dimensional CdS nanostructures: synthesis, properties, and applications, Nanoscale 2 (2) (2010) 168–187.
[11] D. Lang, Q. Xiang, G. Qiu, X. Feng, F. Liu, Effects of crystalline phase and morphology on the visible light photocatalytic H_2 production activity of CdS nanocrystals, Dalton Trans. 43 (19) (2014) 7245–7253.
[12] J. Yu, Y. Yu, P. Zhou, W. Xiao, B. Cheng, Morphology-dependent photocatalytic H_2 production activity of CdS, Appl. Catal. B-Environ. 156–157 (2014) 184–191.
[13] S. Ma, J. Xie, J. Wen, K. He, X. Li, W. Liu, X. Zhang, Appl. Surf. Sci. 391 (2017) 580–591.
[14] H. Yan, J. Yang, G. Ma, G. Wu, X. Zong, Z. Lei, J. Shi, C. Li, J. Catal. 266 (2009) 165–168.
[15] Q. Wang, J. Lian, Q. Ma, S. Zhang, J. He, J. Zhong, J. Li, H. Huang, B. Su, Catal. Today 281 (2017) 662–668.
[16] I. Murillo Leo, E. Soto, F. Vaquero, N. Mota, R.M. Navarro, J.L.G. Fierro, Int. J. Hydrogen Energy 42 (2017) 13691–13703.
[17] Q. Li, X. Li, S. Wageh, A.A. Al-Ghamdi, J. Yu, Adv. Energy Mater 5 (2015) 1500010.
[18] M.B. Mohamed, M.H. Abdel-Kader, A.A. Alhazime, J.Q.M. Almarashi, J. Mol. Struct. 1155 (2018) 666–674.
[19] H. Wei, H. Jiang, Z. Zheng, Q. Zhao, Q. Wu, J. Zhan, Mater. Res. Bull. 48 (2013) 1352–1356.
[20] J. Feng, C. An, L. Dai, J. Liu, G. Wei, S. Bai, J. Zhang, Y. Xiong, Long-term production of H_2 over Pt/CdS nanoplates under sunlight illumination, Chem. Eng. J. 283 (2016) 351–357.
[21] H. Yan, J. Yang, G. Ma, G. Wu, X. Zong, Z. Lei, J. Shi, C. Li, Visible-light-driven hydrogen production with extremely high quantum efficiency on Pt–PdS/CdS photocatalyst, J. Catal. 266 (2) (2009) 165–168.
[22] P. Dalvand, M.R. Mohammadi, D.J. Fray, One-dimensional cadmium sulfide (CdS) nanostructures by the solvothermal process: controlling crystal structure and morphology aided by different solvents, Mater. Lett. 65 (9) (2011) 1291–1294.
[23] A. Hernandez-Gordillo, S. Oros-Ruiz, R. Gomez, Preparation of efficient cadmium sulfide nanofibers for hydrogen production using ethylenediamine (NH2CH2CH2NH2) as template, J. Colloid Interface Sci. 451 (2015) 40–45.
[24] C. Bao, G. Zhu, J. Yang, M. Liu, R. Zhang, X. Shen, Small molecular amine mediated synthesis of hydrophilic CdS nanorods and their photoelectrochemical water splitting performance, Dalton Trans. 44 (3) (2015) 1465–1472.
[25] S. Li, L. Zhang, T. Jiang, L. Chen, Y. Lin, D. Wang, T. Xie, Construction of shallow surface states through light Ni doping for high-efficiency photocatalytic hydrogen production of CdS nanocrystals, Chem. Eur J. 20 (1) (2014) 311–316.
[26] M. Liu, Y. Du, L. Ma, D. Jing, L. Guo, Manganese doped cadmium sulfide nanocrystal for hydrogen production from water under visible light, Int. J. Hydrogen Energy 37 (1) (2012) 730–736.
[27] A. Deshpande, P. Shah, R.S. Gholap, N.M. Gupta, Interfacial and physicochemical properties of polymer-supported CdSZnS nanocomposites and their role in the visible-light mediated photocatalytic splitting of water, J. Colloid Interface Sci. 333 (1) (2009) 263–268.
[28] H. Liu, M. Luo, J. Hu, X. Zhou, J. Li, Synthesis of ZnxCd1-xS solid solution porous spheres as efficient visible-light driven photocatalysts, Sci. Adv. Mater. 5 (9) (2013) 1157–1167.

[29] S.J. Ikhmayies, R.N. Ahmad-Bitar, A study of the optical bandgap energy and Urbach tail of spray-deposited CdS: in thin films, J. Mater. Res. Technol. 2 (3) (2013) 221–227.
[30] H. Khallaf, G. Chai, O. Lupan, L. Chow, S. Park, A. Schulte, Characterization of gallium-doped CdS thin films grown by chemical bath deposition, Appl. Surf. Sci. 255 (7) (2009) 4129–4134.
[31] J. Cai, J. Jie, P. Jiang, D. Wu, C. Xie, C. Wu, Z. Wang, Y. Yu, L. Wang, X. Zhang, Q. Peng, Y. Jiang, Tuning the electrical transport properties of n-type CdS nanowires via Ga doping and their nano-optoelectronic applications, Phys. Chem. Chem. Phys. 13 (2011) 14663–14667.
[32] L. Zhang, Q. Zhang, Y. Luo, Impact of element doping on photoexcited electron dynamics in CdS nanocrystals, J. Phys. Chem. Lett. 8 (2017) 5680–5686.
[33] R. Sasikala, A.P. Gaikwad, V. Sudarsan, N. Gupta, S.R. Bharadwaj, Cubic phase indium doped cadmium sulfide dispersed on zinc oxide: enhanced photocatalytic activity for hydrogen generation from water, Appl. Catal. A-Gen. 464–465 (2013) 149–155.
[34] S. Y lmaz, S.B. T oreli, I. Polat, M.A. Olgar, M. Tomakin, E. Bacaks z, Enhancement in the optical and electrical properties of CdS thin films through Ga and K co-doping, Mater. Sci. Semicond. Process. 60 (2017) 45–52.
[35] S. Mageswari, L. Dhivya, B. Palanivel, R. Murugan, Structural, morphological and optical properties of Na and K dual doped CdS thin film, J. Alloy. Comp. 545 (2012) 41–45.
[36] I.D. Olekseyuk, V.O. Halka, O.V. Parasyuk, S.V. Voronyuk, Phase equilibria in the $AgGaS_2$ ZnS and $AgInS_2$ ZnS systems, J. Alloy. Comp. 325 (2001) 204–209.
[37] I. Tsuji, H. Kato, H. Kobayashi, A. Kudo, Photocatalytic H $_2$ evolution reaction from aqueous solutions over band structure-controlled (AgIn)Zn $_{2(1-x)}S_2$ solid solution photocatalysts with visible-light response and their surface nanostructures, J. Am. Soc. 126 (2004) 13406–13413.
[38] K. Yamato, A. Iwase, A. Kudo, Photocatalysis using a wide range of the visibile light spectrum: hydrogen evolution from doped $AgGaS_2$, Chem. Sus. Chem. 8 (2015) 2902–2906.
[39] D. Briggs, M.P. Seah, Practical Surface Analysis by Auger and X-ray Photoelectron Spectroscopy, Wiley, Chichester, 1990.
[40] M. Haj Lakhdar, T. Larbi, B. Ouni, M. Amlouk, Optical and structural investigations on Sb2S2O new kermesite alloy for optoelectronic applications, J. Alloy. Comp. 579 (2013) 198–204.
[41] G.H. Kim, H.B. Kim, B. Walker, H. Choi, C. Yang, J. Park, J.Y. Kim, ACS Appl. Mater. Interfaces 5 (2013) 1757–1760.
[42] J. Yang, R. Liu, S. Huang, Y. Shao, Y. Huang, Y. Yu, Enhanced photocatalytic activity and stability of interstitial Ga-doped CdS: combination of experiment and calculation, Catal. Today 224 (2014) 104–113.
[43] A. Khorsand Zak, W.H. Abd. Majid, M.E. Abrishami, R. Yousefi, Solid State Sci. 13 (2011) 251–256.
[44] L. Zeiri, I. Patla, S. Acharya, Y. Golan, S. Efrima, Raman spectroscopy of ultranarrow CdS nanostructures, J. Phys. Chem. C 111 (2007) 11843–11848.
[45] C. Hu, X. Zeng, J. Cui, H. Chen, J. Lu, Size effects of Raman and photoluminescence spectra of CdS nanobelts, J. Phys. Chem. C 117 (2013) 20998–21005.
[46] V. Sivasubramanian, A.K. Arora, M. Premila, C.S. Sundar, V.S. Sastry, Optical properties of CdS nanoparticles upon annealing, Physica E 31 (2006) 93–98.
[47] D. Routkevitch, T.L. Haslett, L. Ryan, T. Bigioni, C. Douketis, M. Moskovits, Synthesis and resonance Raman spectroscopy of CdS nano-wire arrays, Chem. Phys. 210 (1996) 343–352.
[48] I. Honma, T. Sano, H. Komiyama, Surface-Enhanced Raman Scattering (SERS) for semiconductor microcrystallites observed in Ag-CdS hybrid particles, J. Phys. Chem. C 97 (1993) 6692–6695.
[49] S. Fateixa, H.I. Nogueira, T. Trindade, Hybrid nanostructures for SERS: materials development and chemical detection, Phys. Chem. Chem. Phys. 17 (2015) 21046–21071.
[50] P.C. Wu, M. Losurdo, Plasmonic gallium nanoparticles on polar semiconductors: interplay between nanoparticle wetting, localized surface plasmon dynamics, and interface charge, Langmuir 25 (2009) 924–930.
[51] C. Wang, E. Yifeng, L. Fan, S. Yang, Y. Li, CdS-Ag nanocomposite arrays: enhanced electro-chemiluminescence but quenched photoluminescence, J. Mater. Chem. 19 (2009) 3841–3846.
[52] T. Abe, Y. Kashiwaba, M. Baba, J. Imai, H. Sasaki, XPS analysis of p-type Cu-doped CdS thin films, Appl. Surf. Sci. 175–176 (2001) 549–554.
[53] C.D. Wagner, A.V. Naumkin, A. Kraut-Vass, J.W. Allison, C.J. Powell, J.R. Rumble Jr., NIST Standard Reference Database 20, Version 3.4 (Web Version), 2003. http:/srdata.nist.gov/xps/.
[54] H.T. Tung, Y. Hwu, I.G. Chen, M.G. Tsai, J.M. Song, I.M. Kempson, G. Margaritondo, Fabrication of single crystal $CuGaS_2$ nanorods by X-ray irradiation, Chem. Comm. 47 (32) (2011) 9152–9154.
[55] R. Carli, C.L. Bianchi, XPS analysis of gallium oxides, Appl. Surf. Sci. 74 (1994) 99–102.
[56] V.K. Kaushik, XPS core level spectra and auger parameters for some silver compounds, J. Electron Spectrosc. Relat. Phenom. 56 (1991) 273–277.
[57] S.K. O'Leary, S. Zukotynski, J.M. Perz, Disorder and optical absolution in amorphous silicon and amorphous germanium, J. Non-Cryst. Solids 210 (1997) 249–253.
[58] K.G. Saw, N.M. Aznan, F.K. Yam, S.S. Ng, S.Y. Pung, New insights on the Burstein-Moss shift and band gap narrowing in indium-doped zinc oxide thin films, PloS One 10 (10) (2015), e0141180.
[59] J. Yang, Y. Jiang, L. Li, M. Gao, Structural, morphological, optical and electrical properties of Ga-doped ZnO transparent conducting thin films, Appl. Surf. Sci. 421 (2017) 446–452.
[60] M. Adelifard, R. Torkamani, Influence of growth temperature and silver to sulfur molar ratios on optical, electrical and thermoelectrical properties of nanostructured Ag_2S thin films, J. Mater. Sci.-Mater. Electron. 26 (10) (2015) 7554–7563.
[61] G. Zhang, D. Monllor-Satoca, W. Choi, Band energy levels and compositions of CdS-based solid solution and their relation with photocatalytic activities, Catal. Sci. Technol. 3 (2013) 1790.
[62] F. Hermann, S. Skilman, Atomic Structure Calculations, Prentice Hall Inc., Inglewood Cliffs, New Yersey, 1963.
[63] H. Tong, N. Umezawa, J. Ye, T. Ohno, Energy Environ. Sci. 4 (2011) 1684.
[64] R. Lozada-Morales, O. Zelaya-Angel, G. Torres-Delgado, On the yellow-band emission in CdS films, Appl. Phys. Mater. Sci. Process 73 (2001) 61–65.
[65] L. Huang, J. Yang, X. Wang, J. Han, H. Han, C. Li, Effects of surface modification on photocatalytic activity of CdS nanocrystals studied by photoluminescence spectroscopy, Phys. Chem. Chem. Phys. 15 (2013) 553–560.
[66] V.K. Singh, P. Chauhan, S.K. Mishra, R.K. Srivastava, Effect of indium doping and annealing photoconducting property of wurtzite type CdS, Electron. Mater. Lett. 8 (2012) 295–299.
[67] P. Thangadurai, S. Balaji, P.T. Manoharan, Surface modification of CdS quantum dots using thiols-structural and photophysical studies, Nanotechnology 19 (2008) 435708.
[68] R.N. Ahmad-Bitar, Effect of doping and heat treatment on the photoluminescence of CdS films deposited by spray pyrolisis, Renew. Energy 19 (2000) 579–586.
[69] T. Mokari, E. Rothenberg, Selective growth of metal tips onto semiconductor quantum rods and tetrapods, Science 304 (2004) 1787.
[70] Y. Li, Y. Ding, H. Liao, Y. Qian, Room temperature conversion route to nanocrystalline mercury chalcogenides HgE (E=S, Se, Te), J. Phys. Chem. Solid. 60 (1999) 965–968.
[71] K. Das, S.K. Panda, S. Gorai, P. Mishra, S. Chaudhuri, Effect of Cu/In molar ratio on the microstructural and optical properties of microcrystalline $CuInS_2$ prepared by solvothermal route, Mater. Res. Bull. 43 (2008) 2742–2750.
[72] J. Feng, J. Han, X. Zhao, Synthesis of $CuInS_2$ quantum dots on TiO_2 porous films by solvothermal method for absorption layer of solar cells, Prog. Org. Coating 64 (2009) 268–273.
[73] S. Shen, L. Guo, X. Chen, F. Ren, S.S. Mao, Effect of Ag_2S on solar-driven photocatalytic hydrogen evolution of nanostructured CdS, Int. J. Hydrogen Energy 35 (2010) 7110–7115.
[74] J.-F. Reber, M. Rusek, Photochemical hydrogen production with platinized suspensions of cadmium sulfide and cadmium zinc sulfide modified by silver sulfide, J. Phys. Chem. 90 (1986) 824–834.